LUND UNIVERSITY

Master Thesis

A numerical comparison of the thermoacoustics for different equivalence ratios for n-dodecane using LES

by

Björn Jarfors

Department of Energy Sciences
Lund University
Sweden
June 19, 2023

Primary Supervisor: **Professor Christer Fureby**
Secondary Supervisor: **PhD-student Arvid Åkerblom**
Examiner: **Professor Xue-Song Bai**

Postal address
PO-Box 118
SE-221 00 Lund, Sweden
Web address
www.energy.lth.se

Visiting address
Ole Römers väg 1

Telephone
+46 46 222 92 80

Printed in Sweden by Media-Tryck.

Lund 2023

Preface

Global warming and climate change is escalating and there is a need to find ways to ensure the future is sustainable. Progress takes time and change is needed immediately. For aero-engines, so-called drop-in fuels are being investigated in order to reduce the carbon footprint of airplanes and fighter jets. These vehicles are very complex and safety is a key parameter which means the research needs to be thoroughly executed before changes are made.

Thermo-acoustics are more prevalent as leaner mixtures are used. This phenomena can create a hazardous operating environment for an aero-engine, leading to a reduced life-time, or engine failure. It can also increase combustion efficiency, as well as reduce emissions. Therefore, the knowledge of this phenomena is desirable. To explore the impact on thermo-acoustic instabilities of drop-in fuels in aero-engines, computational fluid dynamics is used.

Computational fluid dynamics (CFD) is a tool which has been widely used with computational power continuously increasing. The setup of a simulation is not always trivial, and to ensure the quality of the results is satisfactory, it needs to be compared to experimental results. Most experimental results to date are based on fossil fuels. Therefore, a comparison between fossil fuels is the best place to start in order to validate the simulation model. The fuel used is n-dodecane which can act as a surrogate to investigate diesel fuels allowing simpler reaction mechanisms.

I started studying CFD a bit more than a year ago and I have taken several courses to increase my knowledge in this field. I hope my acquired knowledge during this time will help you understand the complex behaviour of thermo-acoustic.

The idea behind this master's thesis was conjured by my secondary supervisor Arvid Åkerblom which I am eternally grateful for as it has been a very interesting subject to study. Coincidentally, this is precisely what will be studied in the new EU-

NEUMANN (Novel Energy and propUlsion systeMs for Air domiNaNce) project which this report will hopefully serve useful for.

To make thermo-acoustics more understandable, a detailed introduction to acoustics is included. I hope you enjoy this reading, and that it makes you as intrigued and but less confused than I have been while writing it.

Regards,
Björn Jarfors
Lund, June 19, 2023

Acknowledgement

I would like to begin by thanking the department of energy sciences for being so welcoming and altruistic. I have had many discussions with faculty members which have enlightened me and conjured up ideas which have helped me during my master's thesis.

I would like to thank Christer Fureby for supplying the case setup and Arvid Åkerblom for organising my thoughts and helping me convey them. Their guidance has been invaluable as they managed to steer my master's thesis in the right direction when things were not clear.

Thank you Robert-Zoltán Szász for setting up my master's thesis computer and helping me get started working with the supercomputer as well as for the debugging and help along the way.

Next I would like to thank two PhD-students, Rasmus Robertsson and Alessandro Ercole for always being happy to help and discuss problems and confusing results.

Special thanks to Tetralith, Dardel and LUNARC for allowing me to use their resources to explore thermo-acoustics.

I would also like to thank my family for putting up with me during my youth, I know it has not been easy!

Lastly I would like to thank my life companion Frida for listening to me talk about thermoacoustics, CFD as well as having the understanding that my mind was always occupied by my master's thesis during this time.

Thank You!

Abstract

Climate change is affecting our world and a more sustainable society is needed. The aviation industry is in need of change but aero-engines are very complex and take time to develop. Thermoacoustic instabilities have the power to destroy an engine, but also to reduce the environmental impact. At the same time, increasing computational power allows detailed simulations to be executed in order to study such complex phenomena. Thermoacoustics is not completely understood yet. With the aid of Large Eddy Simulation's (LES), the thermoacoustics in a bluff-body stabilised flame has been studied for the fuel n-dodecane. A detailed reaction mechanism (SK54) has been used to capture the flame dynamics accurately. Boundary conditions are very important when studying thermoacoustics and a sensitivity analysis has been carried out. The results indicate that the boundary condition for pressure at the outlet is not trivial, and a slight change can both change the excited frequency, as well as the magnitude. A couple of theories have been raised as to why the behaviour changes. One reason could be that the damping changes the speed of sound such that the coupling between heat release due to combustion and velocity perturbations weakens for certain frequencies. This is supported by some literature. Another theory is the change in the input acoustic reactance leading to a certain favoured frequency. Further investigation is needed to verify what the reason is, and how to appropriately set the boundary conditions to obtain results which are in better agreement with experiments.

Sammanfattning

Klimatförändringarna påverkar vår värld och det behövs ett mer hållbart samhälle. Flygindustrin är i behov av förändring, men flygmotorer är mycket komplexa och tar tid att utveckla. Termoakustiska instabiliteter har kraften att förstöra en motor, men också att minska miljöpåverkan. Samtidigt möjliggör ökad beräkningskraft i moderna datorkluster att detaljerade simuleringar kan utföras för att studera sådana komplexa fenomen. Termoakustik är inte helt förstått ännu. Med hjälp av Large Eddy Simulations (LES) har termoakustiken i en bluff-body stabiliserad flamma studerats för bränslet n-dodekan. En detaljerad reaktionsmekanism (SK54) har använts för att fånga flamdynamikens detaljer. Randvillkoren är mycket viktiga när termoakustik ska studeras och en känslighetsanalys har genomförts. Resultaten indikerar att randvillkoret för trycket vid utloppet inte är trivialt, och en liten förändring kan både förändra den exciterade frekvensen, såväl som magnituden. Ett par teorier har tagits upp om varför beteendet förändras. En anledning kan vara att dämpningen ändrar ljudhastigheten så kopplingen mellan förbränningen och hastighetsförändringarna försvagas för vissa frekvenser. Detta stöds av viss litteratur. En annan teori är förändringen i den ingående akustiska reaktansen som leder till en viss favoriserad frekvens. Ytterligare utredning behövs för att verifiera vad orsaken är och hur man på lämpligt sätt sätter randvillkoren för att få resultat som bättre överensstämmer med experiment.

Popular science summary

Our planet is facing a climate crisis that needs to be taken seriously. This calls for researchers and engineers to bring forth new ways to advance society to become more sustainable. One of the industries which need to evolve is the aviation industry which is currently using fossil-based fuels. An idea to decrease the environmental impact due to airplanes and fighter jets, is to use so-called drop-in fuels. It is as it sounds, fuels which we can just drop-in current jet engines. However, the safety in airplanes are of utmost importance. Therefore, there is a need to ensure these drop-in fuels do not cause the engine to break down. You might ask the question, "if it is so difficult, why not just build an electrical airplane?". Well the answer to that question is, "we are not there yet.", and batteries still need rare earth metals to act as a catalyst. Extracting these metal elements also cause harm to the environment.

One of the reasons for an engine to break down, is if so-called thermoacoustic instabilities damage any part of the engine. Thermoacoustics is the coupling between heat release and sound (acoustic field). Heat release feeds energy to the pressure-field (acoustic field) which changes how the flow field will look, which will change the heat release and so on. The heat release amplifies the sound at different frequencies depending on the temperature and geometry. To investigate this, a tool called computational fluid dynamics is used. This means the computational power provided in a computer is used to calculate and simulate flow based on very complicated mathematical equations. Why use a computer and not just create an experiment? Money. It can be a lot cheaper to run a simulation than build an entire experiment.

Since thermoacoustic instabilities are difficult to properly capture, appropriate boundary conditions are needed. These boundary conditions are how we tell the computer to mathematically treat walls, inlets, outlets, and so on. What I found was that the boundary conditions were definitely not trivial to impose. You see, the real outlet, in an acoustic point of view, acts sort of like a spring for particles.

It moves back and forth, and theoretically it has a stiffness and can be extended and compressed a certain length. This behaviour was not easily implemented in the outlet which resulted in both over-predicted and under-predicted results. I believe that it could be because the timing for the energy fed by the heat release to the acoustic field is not correct. This can give some indication of where to look next. A few suggestions are to investigate exactly how the thermoacoustic feedback loop operates and how it changes when altering the boundary conditions. This will require a lot of thought and computer power, but I am optimistic!

Populärvetenskaplig sammanfattning

Vår planet står inför en klimatkris som måste tas på allvar. Detta kräver att forskare och ingenjörer tar fram nya sätt att främja samhället för att bli mer hållbart. En av industrierna som behöver utvecklas är flygindustrin som för närvarande använder fossila bränslen. En idé för att minska miljöpåverkan från flygplan och stridsflygplan är att använda drop-in-bränslen. Det är som det låter, bränslen som vi kan använda direkt i nuvarande jetmotorer. Säkerheten i flygplan är dock av yttersta vikt. Därför finns det ett behov av att säkerställa att dessa drop-in bränslen inte får motorn att haverera. Du kanske ställer frågan, "om det är så svårt, varför inte bara bygga ett elektriskt flygplan?". Svaret på den frågan är, "vi är inte där ännu." och batterier behöver fortfarande sällsynta jordartsmetaller för att fungera som en katalysator. Att extrahera dessa metaller orsakar också skador på miljön.

En av anledningarna till att en motor går sönder är om termo-akustiska instabiliteter skadar någon del av motorn. Termo-akustik är kopplingen mellan värmeöverföringen och ljud (akustiskt fält). Värmeöverföringen tillför energi till tryckfältet (akustiska fältet) vilket ändrar hur flödet kommer att se ut, vilket kommer att ändra värmeöverföring och så vidare. Värmeöverföring förstärker ljudet vid olika frekvenser beroende på temperatur och geometri. För att undersöka detta används ett verktyg som kallas numerisk fluid dynamik. Detta innebär att beräkningskraften som en dator har används för att beräkna och simulera flödet baserat på mycket komplicerade matematiska ekvationer. Varför ska man använda en dator istället för att skapa ett experiment? Pengar. Det kan vara mycket billigare att köra en simulering än att bygga ett helt experiment.

Eftersom termo-akustiska instabiliteter är svåra att avbilda korret behövs lämpliga randvillkor. Dessa randvillkor är hur vi säger åt datorn att matematiskt behandla väggar, inlopp, utlopp och så vidare. Det jag fann var att randvillkor var inte triviala att ställa. Du förstår, det verkliga utloppet, från en akustisk synvinkel, fungerar

som en fjäder för partiklar. Den rör sig fram och tillbaka, och teoretiskt sett har den en styvhet och kan förlängas och komprimeras en viss längd. Detta beteende var inte lätt att implementera vid utloppet, vilket resulterade i både över- och underpredikтera resultat. Jag tror att det kan bero på att tidpunkten för energin som matas av värmeöverföringen till det akustiska fältet inte är korrekt. Detta resultat kan visa vägen om vad som ska undersökas härnäst. Några förslag är att undersöka exakt hur den termo-akustiska återkopplingen fungerar och hur den förändras när man ändrar randvillkoren. Detta kommer att kräva mycket eftertanke och datorkraft, men jag är optimistisk!

Contents

1 Introduction

1.1 Overview

The aviation industry is experiencing increasing pressure to develop ways to become more sustainable. The International Civil Aviation Organization (ICAO) adopted the Carbon Offsetting and Reduction Scheme for International Aviation (CORSIA) which leads to taxation of CO_2 emissions. The idea is for the companies or individuals to fund a reduction of CO_2 emissions elsewhere to reduce the global emissions [1]. This gives incentive to create a more efficient engine, or by changing e.g. to electrical airplanes (assuming the electricity is produced by green methods), or to a more environmentally friendly fuel such as Sustainable Aviation Fuels (SAF) [2]. However, generally the combustor is designed for a specific fuel, and designing these can take a long time, which leads to the need for an intermittent solution, so-called drop-in fuels. The aim is to use more environmentally friendly fuels, which have similar characteristics as current jet fuels to ensure that safe operation is possible. These drop-in fuels will be used in the same combustor as the current jet fuels, and therefore, it is critical to predict what effects these changes will have during operation. Amongst the necessary phenomena that need to be investigated, thermoacoustic instabilities are present. Investigating this will be the focus of this master's thesis.

The purpose of the bluff-body is to help anchor the flame in a combustion chamber or afterburner. The flame is considered anchored if there are incoming cold reactants, which react in the shear layer formed at the trailing edges of the bluff-body. Behind the bluff-body a recirculation zone is formed, which is partly enclosed by the shear layers from the bluff-body. The reactants continue downstream, mixing with hot products and later the mixture is caught in the recirculation zone at the end-of-wake. The recirculation region ensures that incoming reactants have time to combust [3].

Increasing the knowledge of thermoacoustic instability can increase the efficiency of engines and decrease the emissions by allowing the use of more stoichiometric mixtures. Stoichiometric conditions imply that the air-to-fuel ratio is precisely what is needed for the fuel to combust completely. If the conditions are not stoichiometric, one usually refers to the equivalence ratio which is the ratio between the actual air-to-fuel ratio normalised by the stoichiometric air-to-fuel ratio. [4], [5]

In the non-reacting case, right at the trailing edges of the bluff body, Kelvin-Helmholtz (KH) instabilities will be present. This is due to the strong symmetry in the recirculation zone formed in the wake. At the point where the recirculation zone ends, the KH-instability have vortices which roll-up and form a vortex with a certain counter-clockwise, or clockwise-rotating motion. The rotational direction will be periodically decided, and the discharge of these vortices leads to the so-called Bénard/Von Kármán (BVK) instability. These instabilities can be characterized as either absolute instabilities; the instability is self-sustained, no external feeding of energy is needed, or, convective instabilities; the instability requires continuous external feeding of energy. The KH-instability is a convective instability, and the BVK-instability is an absolute instability. [3]

If reactions are turned on, then there will be noticeable heat release in the system. Thus the thermoacoustic instability may be present. This instability is due to the interaction between heat release oscillations, velocity fluctuations and pressure fluctuations. The magnitude of this is usually determined by the Rayleigh Criterion or an extended variant of the Rayleigh Criterion [6]. The heat release is strongly coupled with the acoustic oscillations and flow-field which also affects the distribution of fuel. The feedback loop which is generally discussed includes, heat release oscillations following acoustic oscillations which affects the flow- and mixture perturbations which alters the heat release oscillations which closes the feedback loop. [7]

The heat release affects the vorticity in the system as well. It causes a sudden

change in temperature which leads to a sudden increase in viscosity. The increase in viscosity increases the viscous diffusion, which creates a change in direction for the pressure and density gradients. This initiates the generation of the baroclinic torque, which is present if the density and pressure gradients are misaligned. Also present here is the gas volumetric dilatation. However, the heat release is not homogeneous throughout the system. It is strongly affected by the acoustic oscillations and flow-field which also affects the distribution of fuel. The feedback loop which is generally discussed; flow- and mixture perturbations to heat release oscillations following acoustic oscillations, which affects the flow- and mixture perturbations once again. [3]

Computational fluid dynamics (CFD) has flourished in the past century. It is widely used in research, as well as in the industry. It is based on solving the Navier-Stokes Equations (NSE). However, due to the nature of the turbulent flows, no stable solution exists which causes the requirement to divide CFD into different categories; Direct numerical simulations (DNS), Large eddy simulations (LES), Detached eddy simulations (DES), Reynolds averaged Navier-Stokes (RANS). These have different computational costs, and solution accuracy [8]. In this master thesis, LES will be used due to the unsteady nature of thermoacoustic instabilities. [4]

1.2 Objective

The aim of this master's thesis is to gather a better understanding of the thermoacoustic instabilities present in a bluff body stabilized flame. This will be done numerically with the help of Proper Orthogonal Decomposition (POD), to determine which frequencies are present and carry the most energy [9]. To identify each frequencys' total energy, a fast fourier transform (FFT) will be used in conjunction with the POD. Furthermore, a qualitative comparison between the thermoacoustic instabilities for two different equivalence ratios ($\phi = 0.66$, and $\phi = 0.87$) will be carried out. These equivalence ratios are chosen to have one case in a stable region and

another in the limit-cycle region, as well as being able to compare to the experiment by Paxton et al. [10].

1.3 Constraints

Due to the large computational cost of bluff-body stabilized flames using LES and a detailed set of reactions (SK54), the mesh and internal field is supplied by the supervisor. Furthermore, a mesh sensitivity study has already partly been carried out by the supervisor for propane-air mixtures. [11], [12]

To limit the computational cost, radiative heat transfer is neglected and the reactions are limited to 54 species and 269 reactions. The chosen set of reactions were investigated by the University of California to capture the main dynamics of the flame [13]. Conjugate heat transfer is also neglected, thus the walls are treated as iso-thermal - fixed wall temperature.

Lastly, n-dodecane is a liquid fuel. However, since the inlet boundary condition sets the temperature to 600 K, it is assumed to be fully vaporised.

2 Background

2.1 Benchmarking Article

The purpose of this master's thesis is to shed some light on the changes in thermoacoustics experienced by the system if the equivalence ratio of n-dodecane is altered. This has been studied by Paxton et al. where they experimentally investigated the thermoacoustics for n-dodecane with equivalence ratios between $0.66 \leq \phi \leq 1$. Furthermore, they studied other fuels such as *C-1*, *Jet-A*, *JP-5* as well as *F-24* which is *Jet-A* with *JP-8* additives. [10]

Their setup consists of a rectilinear duct with an equilateral triangular bluff-body. The dry air enters through the back-pressure plate at a mass-flow-rate $w_{air} = 0.35$ kg/s and at 600 K. Shortly downstream the liquid fuel is injected using three fuel spray bars. These are located a short bit downstream from the back-pressure plate. Further downstream, the combustible mixture will be compressed by the bluff-body, and a recirculation zone will develop behind the bluff-body. The large-scale vortices will capture and recirculate the hot burned gas to continuously reignite the shear layer. This can be seen in figure 2.1. If the flame is successfully anchored, it will propagate towards the outlet where it is expanded in a large room. [10]

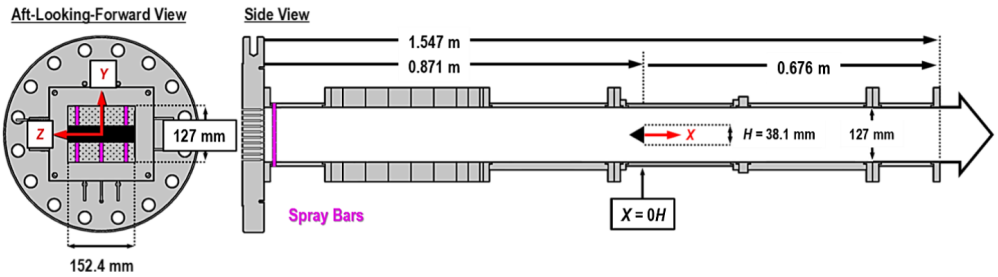

Figure 2.1 – Paxton et al.'s experimental setup. The left most part of the figure demonstates the cross-section of the channel. The side-view is shown to the right, where the flow enters from the left and flows to the outlet present at the far right. [10]

To measure the pressure fluctuations, they used high frequency pressure transducers (HFPT) at different locations. The measuring frequency of these instruments are 40 kHz which they motivate as good enough since their expected dominant longitudinal and transverse resonating frequencies are supposedly below 500 Hz and 5 kHz, respectively. [10]

When increasing the equivalence ratio, the thermoacoustic coupling increase, as well as the overall flame temperature. This leads to an increased temperature at the surface of the bluff-body which increases the preheating of the premixed reactants. This will affect the flow conditions as the bluff-body is not cooled to a specific temperature. Paxton et al. [10] found that the temperature rise of the bluff-body converged to 2 K/min after allowing the heat soak settling time to pass. [10]

Paxton et al. [10] found that the pressure fluctuations as a function of the equivalence ratio was decomposed into three regions; a stable region, transition region and limit-cycle region, which can be seen in figure 2.2 a). The location for which the transition region is entered is called the instability trigger location. The pressure was measured at different regions in the system; at the back-pressure plate and at the trailing edge of the bluff-body. The transition region had a non-linear behaviour as the equivalence ratio was increased. The pressure fluctuations for equivalence ratio $\phi = 0.66$ resulted in pressure fluctuations of approximately 500 Pa, while the fluctuations for equivalence ratio $\phi = 0.87$ resulted in pressure fluctuations of approximately 6.3 kPa. [10]

In figure 2.2 b), a FFT was performed from pressure data-sets measured at the trailing edge of the bluff-body. It can be seen from this figure that the pressure contributions from the different excited frequencies changed as the equivalence ratio was increased. The first longitudinal (quarter-wave) mode increases as the equivalence ratio increases, as well as two double peaks, approximately at the half-wave frequency and slightly below three-quarter-wave frequency. These double peaks merge at equivalence ratio $\phi = 0.87$ and corresponds to a frequency of approximately 230

Hz. Paxton et al. [10] believed that this frequency was the result of the first longitudinal mode from the bluff-body to the combustion chamber's outlet. Furthermore, the first longitudinal modes frequency increased from 91 Hz to 119 Hz as the equivalence ratio was increased from 0.66 to 0.87. They concluded that this is caused by the increased burned gas temperature resulting in a higher speed of sound. Their motivation to this statement is because the burned gas temperature is expected to increase as the equivalence ratio is increased. Their explanation for the increase in pressure fluctuations is that once the system enters the transition region, the frequency begins to lock onto the favoured resonant frequency. They also found that the pressure node is located close to the exit plane, as well as the pressure anti-node being close to the HFPT located a bit downstream of the back-pressure plate. [10]

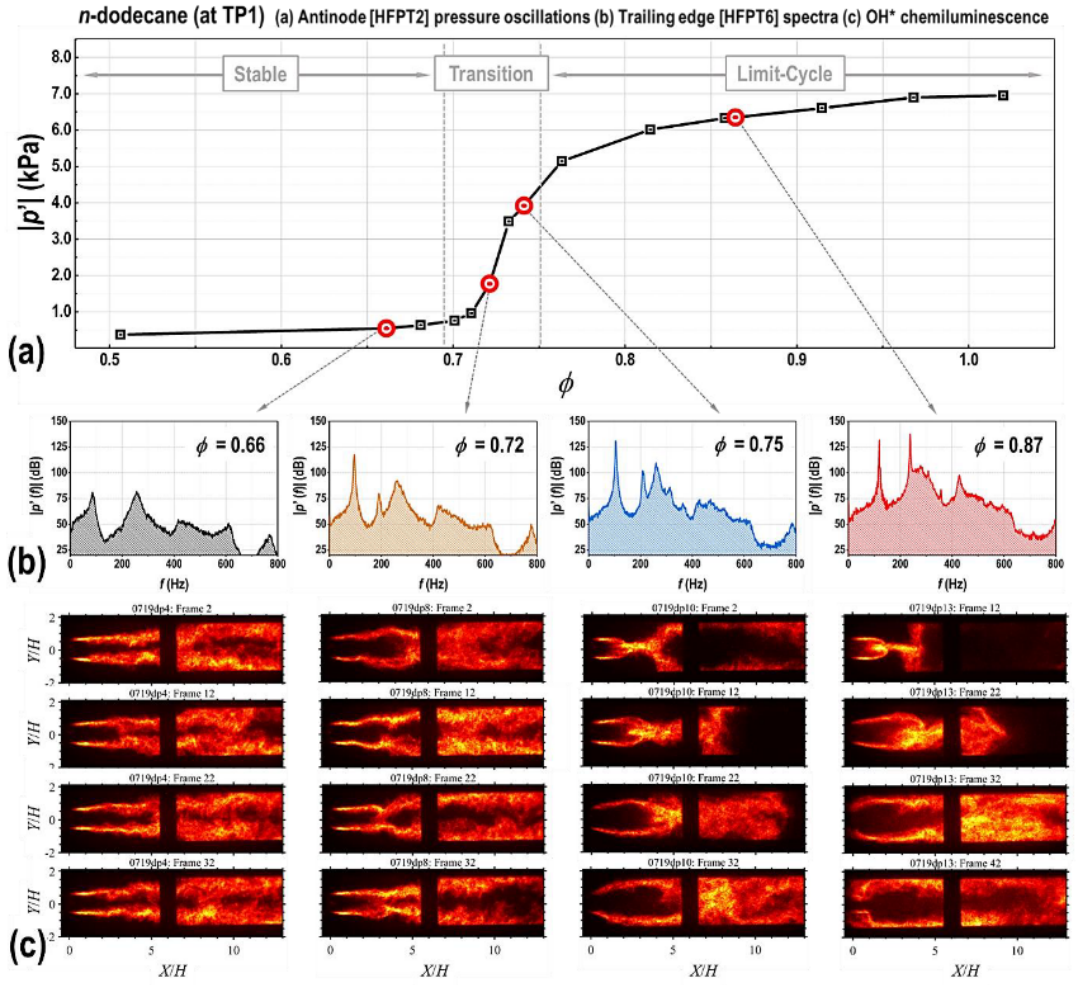

Figure 2.2 – Paxton et al.'s experimental results. The top graph represents the pressure-wave fluctuations magnitude at different equivalence ratios measured at the BPP. Below this graph, the FFT can be found of the pressure-wave fluctuations measured at the BB. Lastly, a few snapshots of the flame-dynamics are shown for the corresponding equivalence ratios used in the FFT. [10]

As mentioned previously, the point for which the stable region and transition region meet, is the so-called instability trigger location. This location is fuel-specific and they found that it seems to have a linear correlation with the derived cetane number (DCN). This translation in the instability trigger location can be seen in figure 2.3. [10]

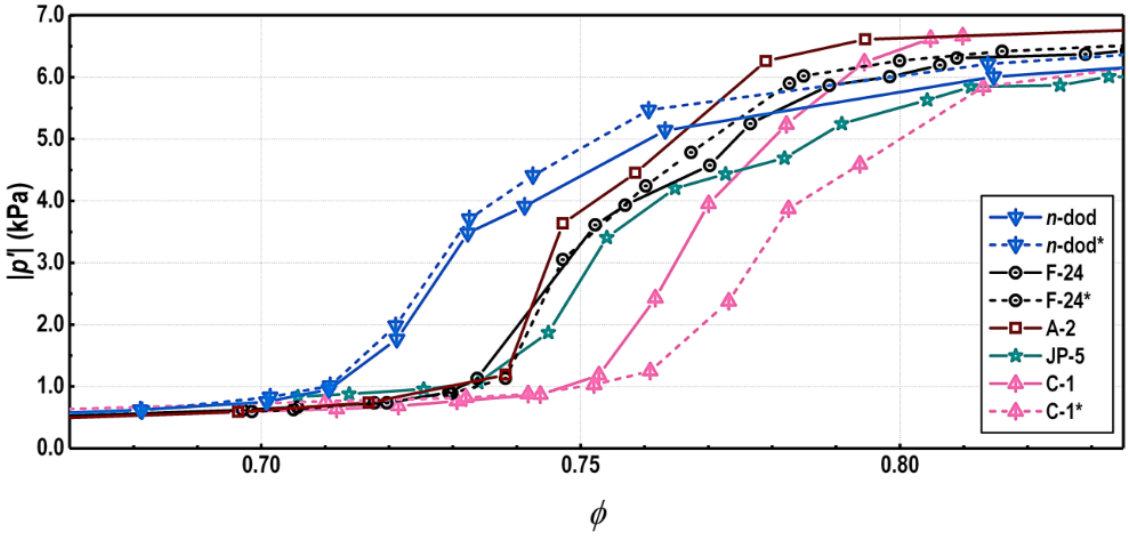

Figure 2.3 – Paxton et al.'s experimental results for the different types of fuel regarding the pressure-wave fluctuations magnitude at different equivalence ratios measured at the BPP. The cases with a '*' indicate the cases which were repeated. [10]

2.2 Instabilities

In general, there are two types of instabilities, convective and absolute. Convective instabilities requires continuous energy to be fed to the instability for it to exist, while absolute instabilities are self-excited. [3]

2.2.1 Bénard/Von Kármán

The Bénard/Von Kármán (henceforth presented as BVK) instability is well-known for its asymmetric, periodic/sinusoidal, shedding of vortices. This instability is considered to be an absolute instability, thus being self-excited. The frequency of the shedding can be estimated by the empirical equation

$$f_{BVK} = \mathrm{St} \cdot \frac{U}{D}, \tag{2.1}$$

where St is the Strouhal number, the value of which depends on the Reynolds (Re) number, and can be seen in figure 2.4, U is the velocity, and D is the diameter of the cylinder bluff-body for which the Strouhal was tabulated. [14]

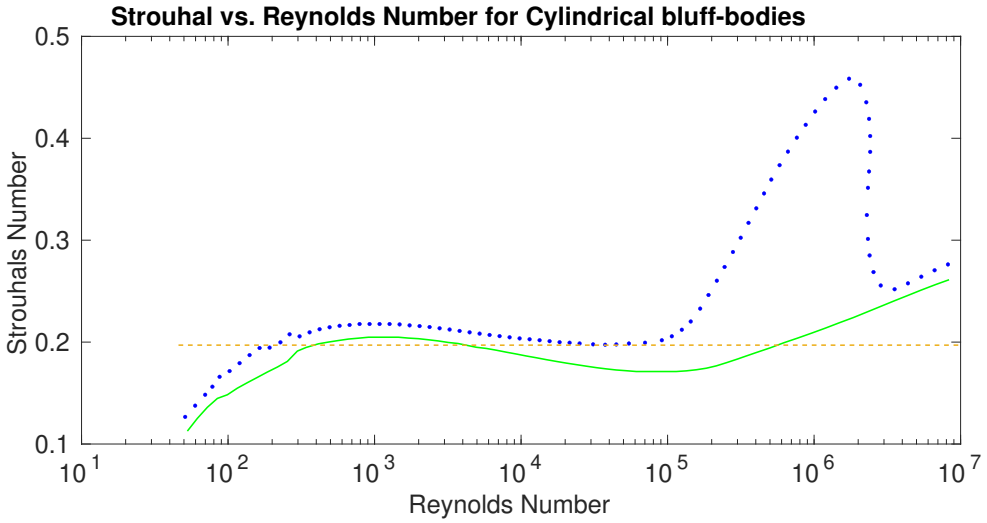

Figure 2.4 – Strouhal number as a function of Reynolds number for smooth and rough surfaces, based on a cylindrical bluff-body. Adapted from Mendez et al. [15]

2.2.2 Kelvin-Helmholtz

The Kelvin-Helmholtz (henceforth presented as KH) instability is more prominent in flows where the burned/unburned gas temperature ratio is higher. It is considered to be a convective instability, and thus it needs to be fed energy to be sustained. The empirically derived equation for the frequency of the KH instability

$$f_{KH} = 0.0235 f_{BvK} \cdot \mathrm{Re}^{0.67}, \tag{2.2}$$

was developed based on the BVK vortex shedding frequency. [14]

2.3 Theory and progress

2.3.1 Bluff-body stabilized flames

Bluff-body stabilized flames have been widely researched by several such as Zukoski [16], Zettervall [17], Fureby [11], [12], [18], Fugger [19]–[21], Paxton [10], [22], and Shanbhogue et al. [3], [14], [23]–[25]. An older experiment done by Sjunnesson and Henrikson [26] in 1992, known as the Volvo Validation Rig, is a classic example of a bluff-body stabilized flame.

The flow enters the rectilinear channel, into an inlet section. The fuel is injected into the flow, and flows through a honeycomb structure in order to straighten and limit the turbulence in the flow. The last step in the inlet section is the seeding injection. Next, the flow enters the combustor section where it will pass and be destabilized by an equilateral triangular bluff-body and combust shortly after. Lastly, the flow will exit into a large room/cavity. [26]

During this experiment, they noticed how the different frequencies present affected the flame-sheet. Low-frequency oscillations led to large scale deformations of the flame sheet, whilst high frequency (roughly 1400 Hz) resulted in a braided sheet structure. A few main conclusions were; shear-layer instabilities control the chemical reactions, and that the different modes are due to acoustic pressure waves interacting with the shear-layer close to the bluff-body flameholder which results in heat release oscillations which in turn close the feedback loop by feeding energy back to the acoustic pressure-waves. [26]

When studying bluff-body stabilized flames, it is interesting to compare a reacting case with a non-reacting (cold) case. The idea of using a bluff-body to stabilize the flame is to create a recirculation zone, which is characterised as a low-pressure region, large vorticle structures and a shear layer. This is present even in the cold case, and thus it is a part of the acoustic field present in the system. [3]

In the reacting case, the reactants flow downstream, passing through the shear layer, and get trapped in the recirculation zone. The reactants will mix with the hot burned gas, increasing the temperature resulting in combustion. If reactions are present in the shear layer, together with reactants moving downstream and getting trapped in the recirculation zone, the flame is considered *anchored*. [3]

The cold case has a couple of clearly visible instabilities present. The previously mentioned BVK-, and KH instabilities which are hydrodynamic instabilities. The KH instability is present in the shear layer, which leads to a vortex roll-up, and

consequently a discharge of larger vortices. This discharge occurs asymmetrically; periodically discharge a vortex with counter-clockwise rotation, followed by a clockwise rotating vortex. If a center-line is drawn from the inlet to outlet, the clockwise vortices will be present in the upper half, and the counter-clockwise vortices in the bottom half. This is the signature of the BVK instability, which is seen as asymmetric vortex-shedding, which is also known as the Von Kármáns vortex street [3]. A typical depiction of vortex-shedding can be seen in figure 2.5

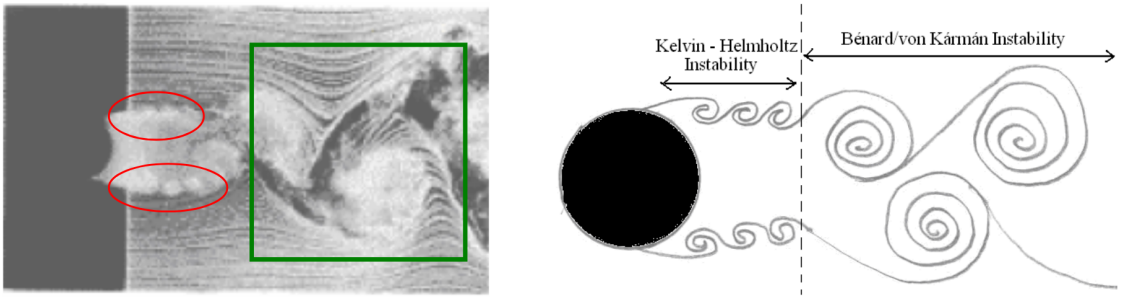

Figure 2.5 – Shear-layer roll-up process, forming a sinousoidal wake. Obtained from [3].

The reacting case will have a more pronounced shear layer which theoretically extends all the way to the outlet, assuming that the flame does not blow out before reaching the outlet. Due to the heat release, the instabilities will differ from the cold case [3]. If there is high heat release, the temperature ratio between burned and unburned gas, T_b/T_u, will increase. Many studies [27]–[29] have shown that this increase will lead to more prominent KH instabilities. These investigations focused on the wake structure behind the bluff-body which resulted in the temperature ratio being linked to whether KH- or BVK instabilities will dominate the flow in the wake.

The key topic of this master's thesis is about thermoacoustic instabilities. These may occur if the heat release fluctuations feed energy to the acoustic field at the right time. A feedback loop between pressure, heat release, and velocity is established, leading to the presence of thermoacoustic instability. Thermoacoustic instability will be described in more detail in a later section. [5], [7], [10]

The development of the vorticity field is well described by Shanbhogue et al. in

[14], [23]–[25], where he goes through the different terms in the vorticity transport equation, when they are dominating and what consequences their dominance will have.

The vorticity transport equation can be derived from the reacting compressible NSE's, using the continuity equation together with the momentum equation, as well as taking the curl of the combined equation followed by a few more algebraic steps. The final vorticity transport equation for reacting compressible flow is

$$\frac{D\boldsymbol{\omega}}{Dt} = (\boldsymbol{\omega} \cdot \boldsymbol{\nabla})\mathbf{v} - \boldsymbol{\omega}(\boldsymbol{\nabla} \cdot \mathbf{v}) - \frac{\boldsymbol{\nabla} p \times \boldsymbol{\nabla} \rho}{\rho^2} + \nu \boldsymbol{\nabla}^2 \mathbf{v}. \tag{2.3}$$

From left to right in equation 2.3, we have the material derivative of the vorticity, vortex stretching, gas expansion, baroclinic production, and viscous diffusion. [23]

Kiel et al. [3] explains how it all begins by introducing heat release from a reaction, which increases the temperature leading to an increase in the molecular viscosity. This will increase the viscous diffusion, which will lead to an inclination of the flame. Since the baroclinic production is dependent the misalignment of the density and pressure gradients, the inclination will lead to such production. In a confined space, the baroclinic torque will counter-act the bluff-body vorticity, and have the same sign as vorticity near the wall. During this process, there will be a substantial amount of gas expansion. The gas expansion, as can be seen by the negative sign in the equation, will reduce vorticity. [23]

The vorticity affects the flame-sheet dynamics, which are very complex. There are a lot of factors which need to be considered when analyzing the flame-sheet dynamics, such as which frequencies are present, and thus which modes are activated. BVK instability is often present if the temperature ratio is not too high between the burned and unburned gases. As mentioned when explaining the reacting case, several researchers [27]–[29] have found that the point for which KH-instability begins to dominate is when this temperature ratio is greater than 2. Moreover, the flame-sheet

interacts with the vorticity and deforms proportionally to the velocity associated by the vorticity, divided by the laminar flame speed, u_ω/S_L. Flame-flame and flame-wall interactions may also occur but will not be covered here. [27]–[29]

A consequence of too much thermoacoustic instability, or a weak flame, is so-called blow-off. The reasons behind the blow-off phenomenon are not completely understood, as there are both linear and non-linear dynamics affecting this. The blow-off velocity can be approximated by $\frac{U_{BO}\tau}{L} = 1$, where U_{BO} is the blow-off velocity, τ is the ignition delay time, and L is the length of the recirculation zone. The ignition delay time is based on the time for a fuel and an oxidiser to react. This is a function of both fuel-type, temperature and pressure. Another equation to determine the blow-off velocity is $U_{BO} = (1 - B_a)\frac{wS_L^2}{\alpha}$, where the blow-off velocity is instead defined as a variable of aerodynamics blockage B_a, aerodynamic wake width w, laminar flame-speed S_L and thermal diffusivity α. For more details you are referred to [30].

There are positive outcomes of thermoacoustic instabilities as well. An example of this is the pulse-combustor which generally has higher efficiency as the burning rates increase due to the increased levels of heat transfer. This also leads to a decrease in emission rates since the species are more often fully combusted. These benefits are of course only useful if there is no damage to the equipment, but also known to decrease the life-time of jet-engines. [4]

As previously mentioned, BVK- and KH-instabilities are hydrodynamic instabilities. These instabilities do not need to have the same frequency as resonance frequency to be excited. Their excitation is already satisfied if their frequency is a multiple of the resonance frequencies. Furthermore, their frequencies may change slightly based on which excited frequencies are present. [4]

2.3.2 Acoustics

In this section some acoustic theory will be introduced, together with a derivation of the wave-equation which was performed by Beranek and Mellow. [31]

Wave Equation

Since thermoacoustic is the coupling of heat release and acoustics, it is important to understand both sides. Acoustics is the study of pressure waves which propagate, and these affect the motion of the fluid. If there are pressure-waves which propagate in both positive and negative directions, these create standing waves. The type of pressure-wave can be distinguished as longitudinal, transverse, azimuthal, and can appear in combination of these in a system. Similar to fluid dynamics and the NSE's, one can use the same method to derive the so-called wave equation. A derivation of the wave-equation following Beranek and Mellows [31] derivation is presented below.

It begins by constructing a cubic control volume with sides Δx, Δy, Δz, and assuming the sound pressure increases from one boundary in each direction, through to the next. Mathematically, they present this as

$$\nabla p = i\frac{\partial p}{\partial x} + j\frac{\partial p}{\partial y} + k\frac{\partial p}{\partial z}, \tag{2.4}$$

where i, j, k are three orthogonal directions which can be any transformation of the original x, y, z directions. This is the change of the pressure in space, also called the gradient of p. To continue, they assume frictionless sides, as well as the internal viscous drag being negligible in comparison to the external viscous drag, one can derive an expression for the external force F, which accelerates the control volume. This is expressed per volume ($V = \Delta x \Delta y \Delta z$). Another reasonable assumption they use is that the mass of the gas in the box is constant. This lets them simplify the equation to

$$\frac{M_{tot}}{V}\frac{D\bar{\mathbf{v}}}{Dt} = \bar{\rho}'\frac{D\bar{\mathbf{v}}}{Dt}, \tag{2.5}$$

where M_{tot} is the total mass of the gas, $\bar{\mathbf{v}}$ is the average velocity vector of the gas,

and $\bar{\rho}^{'}$ is the space average of the instantaneous gas density. Next they rewrite equation 2.5 assuming small fluctuations in the sound waves as well as the material derivative $D\mathbf{v}/Dt \approx \partial\bar{\mathbf{v}}/\partial t$ results in

$$-\nabla p = \rho\frac{\partial\bar{\mathbf{v}}}{\partial t}, \tag{2.6}$$

which is known as the equation of motion.

Their next step is to rewrite the gas law. They begin by assuming the audible range of frequencies are adiabatic and approximating the pressure fluctuations to be less than 110 dB. This allows them to rewrite the gas law

$$\frac{p}{p_0} = -\frac{\gamma V^{'}}{V_0}, \tag{2.7}$$

where p_0 is the mean pressure, γ is the ratio of specific heat capacities, $V^{'}$ is the volume fluctuations and V_0 is the mean volume. Taking the time derivative

$$\frac{1}{p_0}\frac{dp}{dt} = -\frac{\gamma}{V_0}\frac{dV^{'}}{dt}. \tag{2.8}$$

Next they derive the wave equation using the continuity equation, assuming that the mass in the box remains constant. This is done in rectangular coordinates together with the gas law

$$\frac{\partial p}{\partial t} = -\gamma p_0 \nabla\cdot\bar{\mathbf{v}}. \tag{2.9}$$

Differentiating once more with respect to time

$$\frac{\partial^2 p}{\partial t^2} = -\gamma p\nabla\cdot\frac{\partial\bar{\mathbf{v}}}{\partial t}. \tag{2.10}$$

This is followed by taking the divergence of equation 2.6 and using the laplacian

$(\nabla \cdot (\nabla p) = \nabla^2 p)$

$$\nabla^2 p = \frac{\rho_0}{\gamma p_0} \frac{\partial^2 p}{\partial t^2} \longrightarrow$$
$$\nabla^2 p - \frac{1}{c_0^2} \frac{\partial^2 p}{\partial t^2} = 0. \tag{2.11}$$

[31]

From the wave-equation, different expressions can be obtained. As done by Beranek and Mellow [31], an expression for the specific acoustic impedance

$$Z_S = \frac{p(x,t)}{v(x,t)} = \rho_0 c, \tag{2.12}$$

was obtained.

Another interesting impedance to investigate is the impedance which an open-end inputs into the system. The idea is that the open-end can be seen as a moving piston. This applies to a channel with one rigid-closed end and one open-end. The acoustic impedance is

$$Z_A = -j \frac{\rho_0 c}{\pi a^2} \cot k l', \tag{2.13}$$

where $a = r$ for a circular tube, and $a = \sqrt{\frac{S}{\pi}}$ for a rectangular tube, where S is the cross-sectional area of the tube, l' is the length until the termination of the tube. [31]

Since the assumptions affect the end results, below are a couple of variants which will not be derived here, which are derived by Poinsot and Veynantes [4]. For non-reacting flows, a term responsible for turbulent flow noise $-\gamma p_0 \nabla \mathbf{v} : \nabla \mathbf{v}$ is included. A chemical heat release term is included for the reacting flows $(\gamma - 1)\frac{\partial \dot{\omega}_T}{\partial t}$ where $\dot{\omega}_T$

is the heat release. In their complete form:

$$\nabla^2 p - \frac{1}{c_0^2}\frac{\partial^2 p}{\partial t^2} = -\frac{\gamma p_0}{c_0^2}\nabla \mathbf{v} : \nabla \mathbf{v}, \;\; non - reacting, \tag{2.14}$$

$$\nabla^2 p - \frac{1}{c_0^2}\frac{\partial^2 p}{\partial t^2} = \frac{(\gamma - 1)}{c_0^2}\frac{\partial \dot{\omega}_T}{\partial t} - \frac{\gamma p_0}{c_0^2}\nabla \mathbf{v} : \nabla \mathbf{v}, \;\; reacting. \tag{2.15}$$

For a list of all the assumptions, you are referred to chapter 8 in [4].

Acoustics in tubes and different geometrical channels have been widely researched. The simple arbitrary case of a channel with two ends can consist of; closed-closed, open-closed/closed-open, open-open.

A common way to characterise different waves is by using the terms; nodes and anti-nodes. Nodes being where the pressure fluctuations or displacement is zero. When the anti-node represents the fluctuations maximum or minimum, it is known as the crest and trough of the wave, respectively. Since the pressure is generally maximum where the displacement is zero, there is a need to distinguish between displacement fluctuation nodes and pressure nodes. On the opposite side, there are anti-nodes which refer to the maximal pressure fluctuation or maximum displacement fluctuation. These will be referred to as displacement anti-nodes, and pressure anti-nodes.

The cases of open-open and closed-closed are similar in the way that there are either two pressure nodes at the channels ends (open-open), or two displacement nodes (closed-closed). If the channel consists of one closed-end and one open-end, e.g. as in figure 2.7, then the two ends will have a displacement node and a pressure node, respectively. Due to this, the first longitudinal wave will be either a half-wave (open-open or closed-closed), or a quarter-wave (closed-open). Furthermore, while the open-open and closed-closed channels may have all harmonics; first, second, third, nth. The closed-open channels may only have odd harmonics; first, third, $2n + 1$. Thus the equations to determine the frequency of the first longitudinal

mode will differ by a factor two, and are

$$f_{1,0,0} = \frac{c}{4l'} \;\; for \;\; closed - open \;\; channels, \tag{2.16}$$

$$f_{1,0,0} = \frac{c}{2l'} \;\; for \;\; closed - closed/open - open \;\; channels, \tag{2.17}$$

where the indices on the frequency stands for the normal vector from the plane for which the wave propagates. $(1, 0, 0)$ corresponds to the first longitudinal wave in the axial direction, and $(3, 0, 0)$ would correspond to the third longitudinal wave in the axial direction. Furthermore, c is the speed of sound, which equals $\sqrt{\gamma RT}$ (for ideal gas), where γ is the ratio of specific heats, R is the specific gas-constant ($\frac{R_A}{M}$, $R_A = 8.314$ is the universal gas constant, and M is the molar mass of the gas mixture) and T is the absolute temperature. [32],[33]

Acoustic Components

The acoustic components consist of acoustic mass, acoustic compliance and acoustic impedance. The real part of the acoustic impedance corresponds to the resistance, and the imaginary part corresponds to the reactance. Note that the imaginary part is not present in travelling waves, but it is present in a standing wave [34]. Acoustic masses for channels which has one or two open ends which leads to a large domain, such as a cavity, go through a transition from one organised status, to another. This can be translated as an extension of the channel

$$l_{end} = \frac{M_{A1}\pi a^2}{\rho_0} = \frac{8a}{3\pi} \tag{2.18}$$

where M_{A1} is the acoustic mass, a is the characteristic length of the channel (radius for a tube, and $\sqrt{S/\pi}$ for a non-round tube where S is the cross-sectional area of the tube), ρ_0 is the density of the gas. For more detailed derivation of these parameters, see Beranek and Mellow [32]. An illustration of the end-correction by [35] can be seen in figure 2.6.

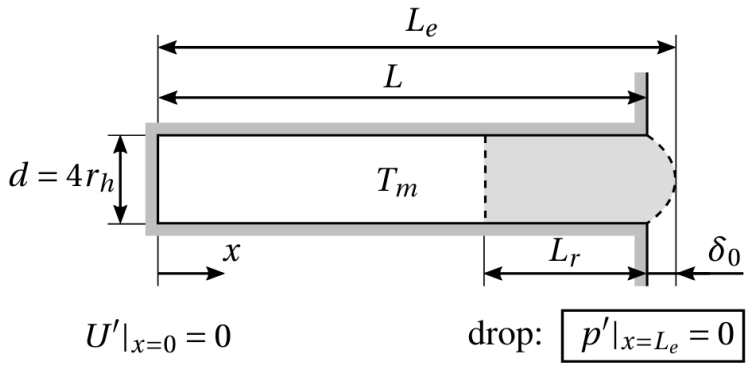

Figure 2.6 – Representation of the end-correction ($\delta_0 = l_{end}$) and an example of how the dispersion occurs when transitioning from one cross-section to another. Obtained from [35].

In order to determine the input acoustic impedance at the open-end of a duct, equation 2.13 can be used if the sidewall friction may be neglected ($r > 0.05/\sqrt{f}$) as well as the lateral standing waves not being present ($r < 10/f$).

2.3.3 Flame-Acoustic Interactions

The acoustics and turbulent combustion interact even for stable cases. Therefore, the boundary conditions are of extreme importance to capture the acoustics correctly. Determining boundary conditions to adequately solve the correct amount of reflection and transmission are of utmost importance. There will be two waves, one entering the channel, and one exiting as depicted in figure 2.7.

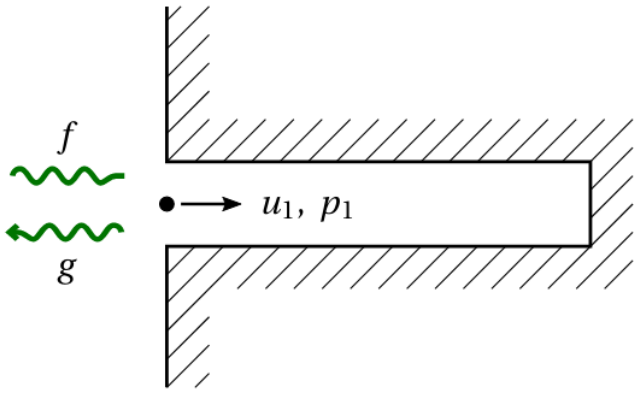

Figure 2.7 – Quarter-wave resonator demonstrating reflected wave f re-entering the channel, and transmitted wave g exiting the channel. Obtained from [35].

Previously in the acoustics subsection an end-correction was mentioned. This end-correction may vary with combustion. An example of how the propane-air flame extends beyond the outlet into a large room is shown in figure 2.8 by [22].

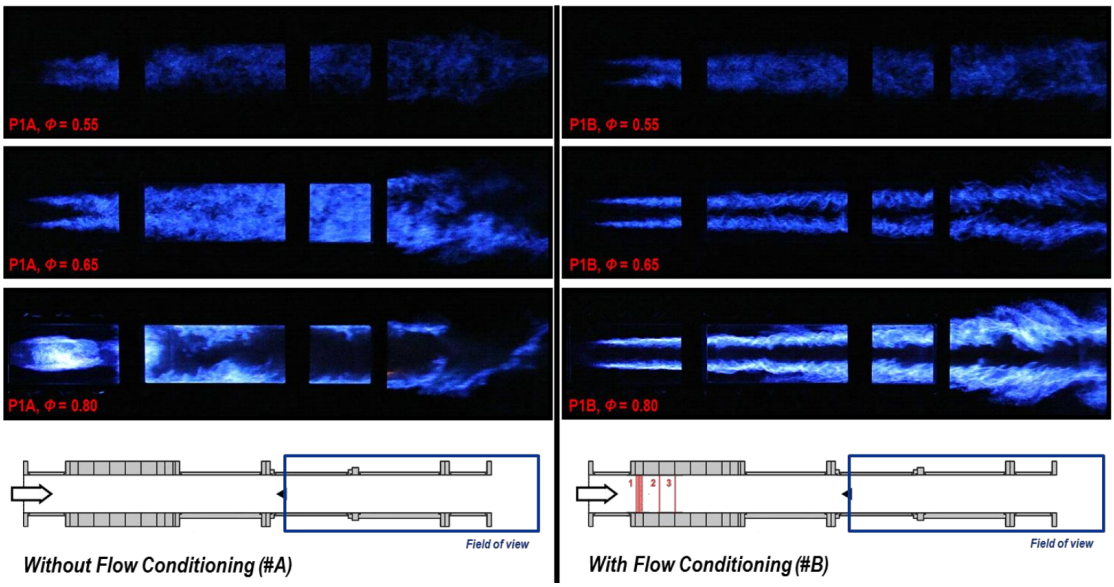

Figure 2.8 – Snapshot of a bluff-body stabilized flame with propane as fuel for different equivalence ratios. The left set of snapshots are without flow-conditioning, and the right set of snapshots are with flow-conditioning. Obtained from [22].

2.3.4 thermoacoustics

The acoustic theory presented above do not include any heat release e.g. due to combustion. If combustion occurs in a system with an acoustic field, the combustion will create spherical waves which propagate according to the gas expansions interaction with the acoustic field (or pressure field for a more intuitive understanding). As Shanbhogue et al. [3], [14], [23]–[25] mentioned so well by connecting the transport equation for vorticity with combustion.

thermoacoustic instabilities become more apparent the leaner the mixture becomes. To reduce emissions, leaner mixtures are needed. Therefore, the understanding of thermoacoustic instabilities are vital in order to reach these milestones. [5]

When two species react and combust, it passes through different stages of combustion: preheat layer, inner layer, and an oxidation layer. Therefore, it is not correct

to simply assume a global reaction, e.g. n-dodecane completely combusts and immediately produces carbon dioxide and water. However, these reaction mechanisms are extremely complex for jet fuels with several thousands of reaction steps. Therefore, it is of interest to pick the most important reaction steps to accurately predict the combustion at hand as well as reducing the cost.

It has been found to be important to include radical species such as carbon monoxide (CO), hydroxide (OH), formaldehyde (CH_2O), aldehyde (HCO) and more. CO increases gradually in the preheat layer, inner layer, and in the oxidation layer (idealy) carbon monoxide oxidates to carbon dioxide. A similar transition occurs for formaldehyde, therefore these can be used as markers to see where the oxidation layer is located. This is more accurately described by Zettervall, et. al in [17] where they use 66 (Z66) reaction steps to describe propane combustion. They also mention how these radicals affect the prediction of ignition delay time and extinction strain-rate.

The time delay is one of the parameters which is important to accurately predict in order to get the correct thermoacoustic behaviour. This is describe by Candel et. al [36] and Poinsot and Veynante in [4]. They describe the equation for stability using the $n - \tau$ formulation which is based on assuming the combustion to only be dependent on the amplitudes of the pressure-waves (A, B, C, D). The equation to determine if the system is stable is

$$\zeta \cos k_1 a \cos k_2 b - \sin k_1 a \sin k_2 b \left[1 + n \exp i\omega\tau\right] = 0, \tag{2.19}$$

where $\zeta = \frac{\rho_1 c_1}{\rho_2 c_2}$ is the specific acoustic impedance, where the index 1 stands for the region where the gas has not entered the reaction zone (before bluff-body) and index 2 is the region where the gas is in the reaction region (and begun reacting). The density is coupled with the pressure which is calculated using the following equations

for respective region:

$$p_1(x,t) = A\exp\left(ik_1(x-a) - i\omega t\right) + B\exp\left(-ik_1(x-a) - i\omega t\right), \tag{2.20}$$

$$p_2(x,t) = C\exp\left(ik_2(x-a) - i\omega t\right) + D\exp\left(-ik_2(x-a) - i\omega t\right), \tag{2.21}$$

where $k = \omega/c$ is the wave number. The coefficients (A, B, C, D) in front of each exponential are simply the different amplitudes of the acoustic traveling waves. These are determined based on the reflection coefficient which tells us the fraction of the travelling wave will be reflected $R = A/B$. R can be determined based on the impedance at the reflective/partially reflective boundaries. This is done by analyzing the impedance at the boundary, i.e. a duct connected to a large cavity with a fixed pressure such that the pressure fluctuations are zero leads to $R = -1$ and $Z = 0$. Note that $R = \frac{Z+1}{Z-1}$. [36], [37]

If the velocity perturbations at the bluff-body flame holder are said to be the driving mechanism for the perturbations in the heat release, then a simple scaling law can be used to derive an expression coupling $\dot{Q}_1$ and v_1 as such

$$(\gamma - 1)\frac{\dot{Q}_1}{\rho_1 c_1^2} = \mathrm{S}n\exp(i\omega\tau)v_1(a), \tag{2.22}$$

where $\dot{Q}_1$ is the unsteady heat release, S is the Rayleigh index, and τ is the time delay. The equation for pulsation ω can be derived from equation 2.22

$$\cos(k_1 a)\cos(k_2 b) - \Gamma\sin(k_1 a)\sin(k_2 b)(1 + n\exp(i\omega t) = 0, \tag{2.23}$$

where $\Gamma = (\rho_2 c_2 S_1)/(\rho_1 c_1 S_2)$, where the indices indicate the values prior to the bluff-body (1), and the values after the bluff-body (2). [4]. This is simplified to the following equation:

$$\cos(2ka) = \frac{1}{2}n\exp(i\omega\tau). \tag{2.24}$$

To derive an indication of instability from equation 2.24, the following is done: Firstly, $n > 0$ which indicates there is combustion. Secondly, this leads to the

variable wave number k, which can be expressed as a a sum of the mean value, and the fluctuating value, $k = k_0 + k^{'}$ [4]. The real part and imaginary part of $k^{'}$ are split and are as follows:

$$Re(k^{'}) = -\frac{n}{4a}\cos(\omega_0 \tau) \tag{2.25}$$

$$Im(k^{'}) = -\frac{n}{4a}\sin(\omega_0 \tau). \tag{2.26}$$

[4] The acoustic modes are said to be unstable if $Im(k^{'}) > 0$. [37] Thus they are unstable if

$$\left(m - \frac{1}{2}\right) T_0 < \tau < mT_0, \tag{2.27}$$

where the acoustic-mode's time-period for the first longitudinal mode is defined as $T_0 = 8l^{'}/c$, and m is an integer. [4]

The same can be done for the third longitudinal mode which results in:

$$\left(m - \frac{1}{2}\right) T_1 < \tau < mT_1, \tag{2.28}$$

where the acoustic-mode's time-period for the third longitudinal mode is defined as $T_1 = 8l^{'}/3c$ [4]. If these two conditions are combined, figure 2.9 can be obtained. [4]

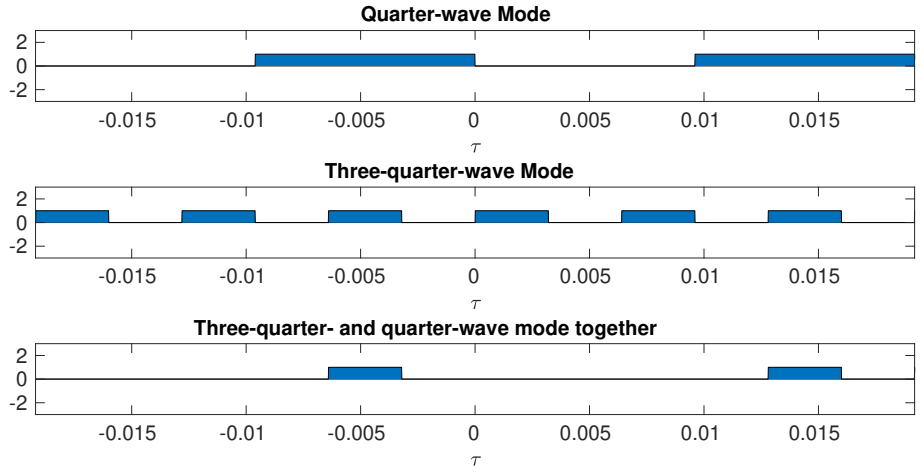

Figure 2.9 – The bars for the quarter-wave, three-quarter-wave and the combined waves are presented from top to bottom. The bars represent when each mode is stable. This figure is adapted from Poinsot and Veynante [4].

To analyze the thermoacoustics in a system, different criterion's have been derived and improved over the years. The most famous one is the Rayleigh Criterion derived back in 1878 which states that, if the sum of the product between the pressure (p_1) and heat release fluctuations (q_1) in the system is larger than zero, the combustor (system) is unstable. However, this is not completely true since there are losses in the system which the fluctuations need to overcome. Thus an improved version is if the same sum of products is larger than the sum of acoustic losses at the boundaries. The entropy is not included in this criterion, which has been argued by Nicoud and Poinsot [6] that if heat release, such as a consequence of combustion is present, this criterion leads to certain discrepancies. The Rayleigh criterion and two extended versions are

$$\iiint_\Omega p_1 q_1 \, d\Omega > 0, \tag{2.29}$$

$$\iiint_\Omega \frac{\gamma - 1}{\gamma p_0} p_1 q_1 \, d\Omega > \iint_\Sigma p_1 \mathbf{u}_1 \cdot \mathbf{n} \, d\Sigma, \tag{2.30}$$

$$\iiint_\Omega \left(\frac{T_1 q_1}{T_0} - \frac{P_0}{r C_p} s_1 \mathbf{u}_1 \cdot \nabla s_0 \right) d\Omega > \iint_\Sigma p_1 \mathbf{u}_1 \cdot \mathbf{n} \, d\Sigma, \tag{2.31}$$

where C_p is the specific heat capacity at constant pressure, s_1 is the entropy fluctuations and s_0 is the entropy of the mean flow. Note that the volume integral is taken

for the entire combustor, Ω, and the acoustic losses area integral is taken from the normal of the boundaries, Σ. [6]

Other ways to characterise the thermoacoustic instabilities in bluff-body stabilized flames have been investigated by Kostka et al. [9] using Proper Orthogonal Decomposition (POD). They found that using POD on pressure is a viable method to quantitatively investigate the shedding contributions for different conditions in the system. The different conditions include equivalence ratios between 0.6 and 1.1. [9]

Their experimental study observed how the energy contained in different modes were divided into three categories: uncorrelated energy, symmetric energy and asymmetric energy. BVK instability is connected to the asymmetric energy and KH is connected to the symmetric energy. Some of their results can be seen in figures 2.10 and 2.11. [9]

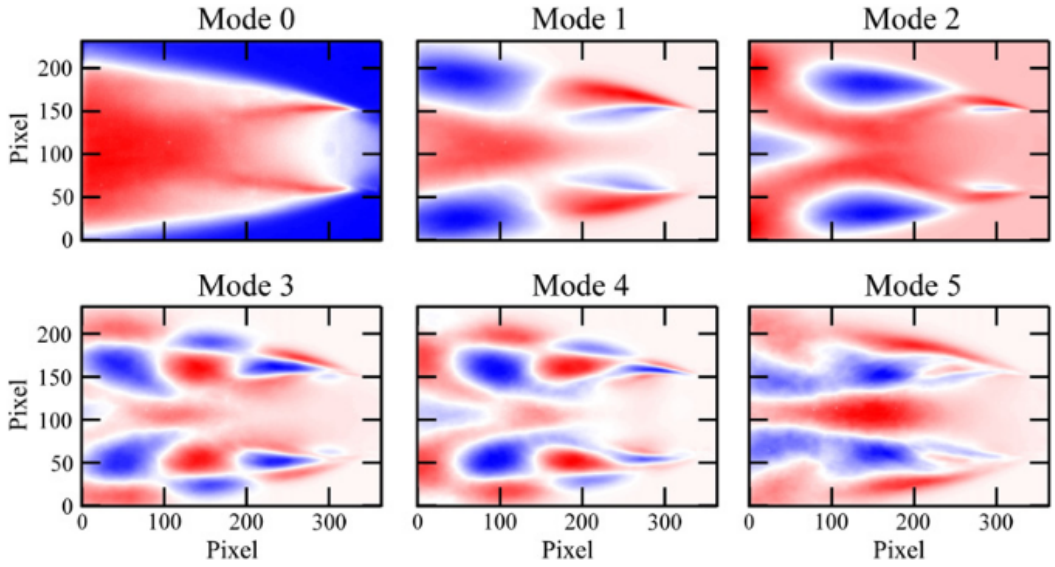

Figure 2.10 – POD of high-speed chemiluminescence imaging which were taken to analyze the symmetric and asymmetric energy. This was done for the v-gutter bluff-body at stoichiometric conditions ($\phi = 1$). Obtained from [9].

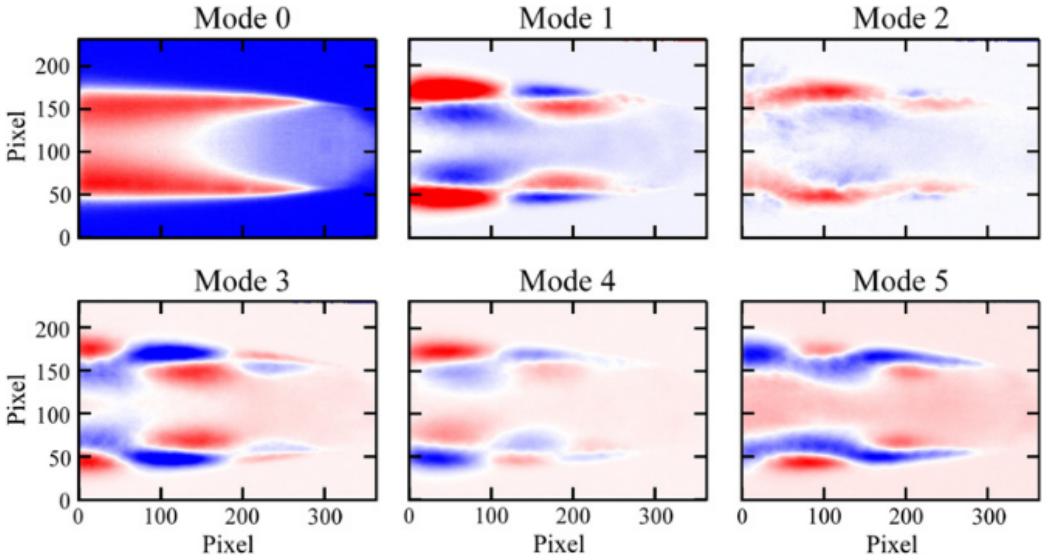

Figure 2.11 – POD of high-speed chemiluminescence imaging which were taken to analyze the symmetric and asymmetric energy. This was done for the v-gutter bluff-body at rich conditions ($\phi = 0.7$). Obtained from [9].

By using POD they found that the symmetric energy increased with equivalence ratio, and the asymmetric energy decreased. This indicated that the KH instability begins to dominate over the BVK instability for higher equivalence ratios which is due to the increased temperature ratio between burned and unburned gases [9].

A recent study from 2020 was done by Tomlin et al. [38] which included 5 different cases. The different cases were set-up while maintaining the bluff-body blockage-ratio with the focus on thermoacoustic instabilities. The bluff-body blockage-ratio is defined as the ratio between the maximum height of the bluff-body, and the total height of the channel. The cases can be seen in the list below:

Case 1. vitiated flow with a configuration of three bluff-bodies with a small 2. spacing between each other,

Case 3. unvitiated flow with a configuration of three bluff-bodies with a small spacing between each other,

Case 4. vitiated flow with a configuration of three bluff-bodies with a larger spacing between each other,

Case 5. vitiated flow with a configuration of a single bluff-body,

Case 6. unvitiated flow with a configuration of a single bluff-body.

Their results showed for an equivalence ratio of 1.0, unvitiated flow has a higher amplitude in their pressure fluctuations than vitiated flow. They argue that unvitiated flow with a single bluff-body has the highest amplitude. However, their comparison has an equivalence ratio of 0.9 instead of 1.0 and thus these effects could cause a different response. They used POD on OH^* chemiluminescence images and coupled it with FFT to include which excited frequencies are present in the different POD modes. This can be seen in figure 2.12 below. [38]

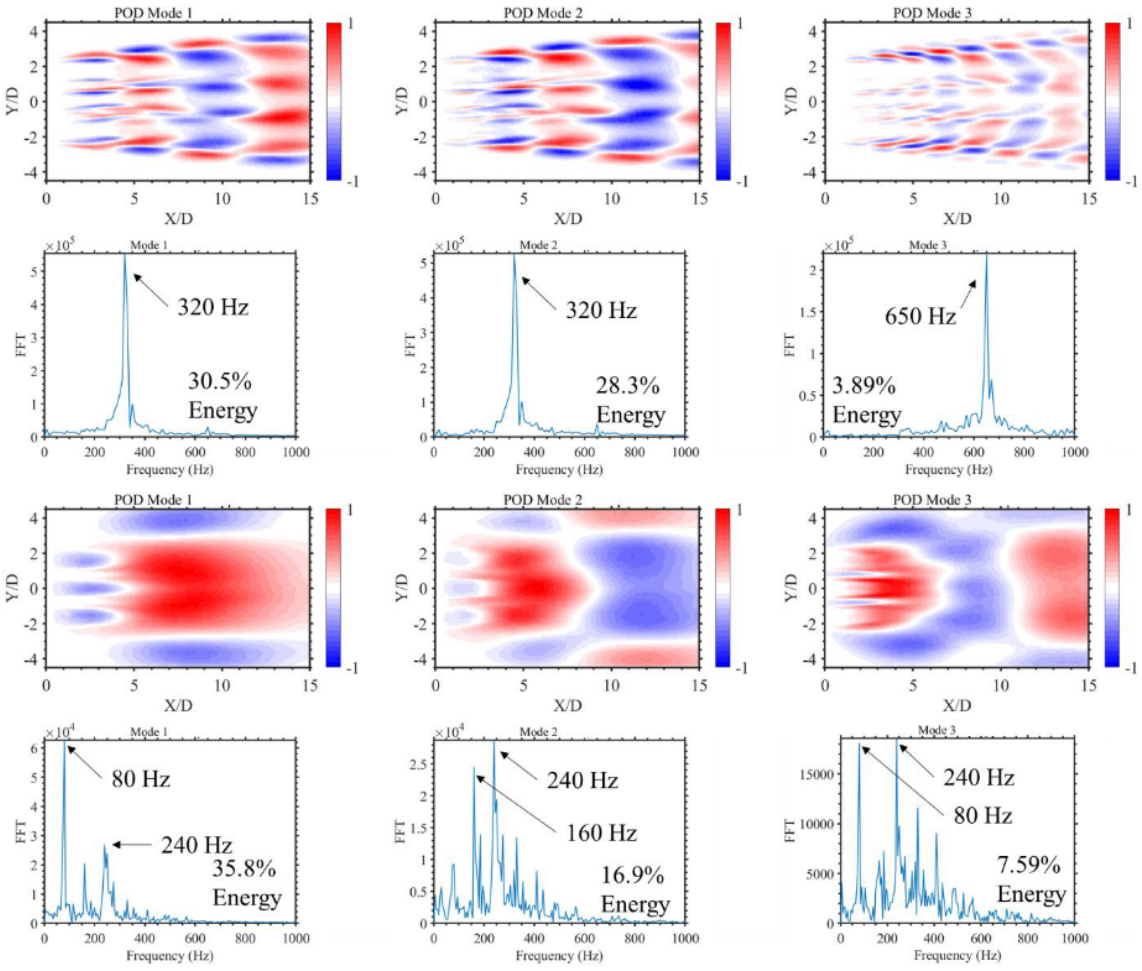

Figure 2.12 – POD on high-speed chemiluminescence imaging for three-bluff bodies with vitiated flow with small spacing at the top, unvitiated flow with small spacing at the bottom. These POD images were paired with a FFT. Obtained from [38].

Another study carried out by Zettervall et al. [17] used POD for the velocity dataset when studying global and skeletal reaction mechanisms for bluff-body stabilized flames. This approach allowed them to analyze the velocity energy distribution in the different Proper Orthogonal Modes (POM). This can be seen in figure 2.13. [17]

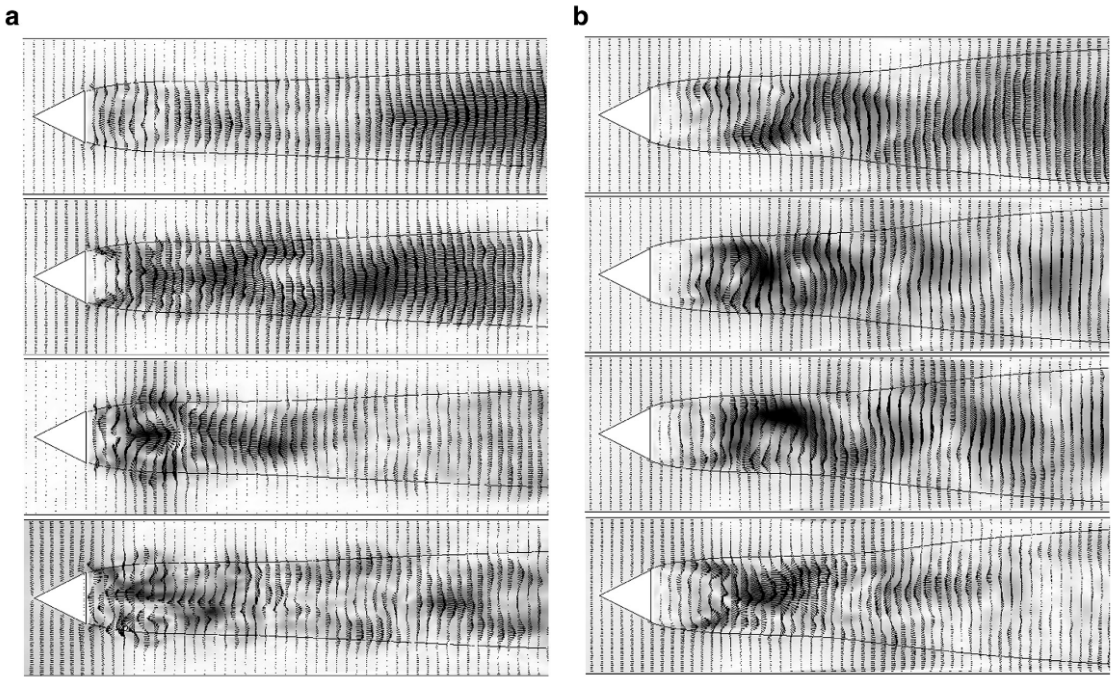

Figure 2.13 – POD of the velocity shown by the gray-scale vector field with a superimposed average temperature contour of 1200 K. The left images are of case 1's four first POD modes, and right images are of case 2's four first POD modes. Obtained from [17].

POD is used to separate a system into a summation of a set of coherent structures (linear combination of snapshots). In general, these coherent structures are represented by a symmetric colorbar. A system can have many POM. However, only a few with correspond to the majority of the systems total energy. Therefore it is common to only look at i.e. the first four modes for pressure. These modes will correspond to different travelling waves which can be dominated by a single frequency or a combination of several frequencies [9]. Following the process described by Kostka et al. [9], the POD decomposition begins by decomposing the snapshots into a correlation matrix and then solving the eigenvalue problem. This matrix is a

square matrix and is computed using

$$C_{ij} = \int_{\Omega} u_i^*(x) u_j(x) dx, \tag{2.32}$$

where the asterix symbolizes the conjugate and u_i, u_j are image sets, where the indices i, j indicate the temporal image frames. Once the correlation matrix is obtained, the eigenvalue problem is solved

$$\boldsymbol{CA} = \lambda \boldsymbol{A}. \tag{2.33}$$

To obtain the POM, the spatial information must be combined with the eigenvalues so that the POM may be reconstructed as follows:

$$\phi^{(n)}(x) = \frac{1}{\lambda^{(n)} N_T} \sum_{j=1}^{N_T} a_j^n u_j(x), \tag{2.34}$$

where $\phi^{(n)}$ are the POD modes, λ and a are the eigenvalues and eigenvectors and lastly N_T is the dimension of the square matrix.

Another mathematical tool which can be used to analyze the acoustics and thermoacoustics is FFT. FFT is a discrete FT (DFT), which means that it is based on datasets and not functions [39]. To use DFT correctly, there is a need for the sampling frequency to be double that of the studied frequencies [40]. If the sampling frequency is too low, the high frequencies may show up as low frequency artifacts. [39], [40]

2.3.5 Boundary Conditions

As mentioned above, boundary conditions (BCs) are vital for accurate predictions of combustion instabilities. In the acoustic and thermoacoustic theory sections the end-correction and impedance at the boundaries were mentioned. Apparent in the literature [4], [37], it is not appropriate to impose a fixed pressure also known as a Dirichlet BC (DBC) for the outlet. This is due to the reflective nature of such

a boundary. Instead the acoustic waves need to be transmitted, i.e. based on a reflection coefficient measured in experiments which consists of both real and imaginary parts. [4]

A common way to analyze what BC's are necessary, is to check which way information flows. There are three vectors for information to flow which have different wave-speeds and are defined as $v - c$, v, $v + c$. For each information vector pointing into the system, a DBC needs to be defined. For example, for supersonic inlet and outlet, all vectors will point in at the inlet, and out at the outlet. Therefore, there is a need for three DBCs at the inlet, but no DBCs for the outlet. A subsonic inlet and outlet, will need two DBCs are need at the inlet, and one at the outlet. However, setting a strict DBC for pressure at the outlet, will lead to a reflective BC. A common way to solve this is to used a mixed BC, also known as a Robin BC (RBC). This is a combination of a DBC and a Neumann BC (NBC, which is a gradient BC) [4], [37]. The result of this is the OpenFOAM BC of type 'waveTransmissive'. It is based on Linear One-Dimensional Inviscid flow (LODI) [41]. This involves transmitting one-dimensional waves, thus the rest will be reflected. However, if the flow is predominantly in one direction, this assumption is valid. For a more detailed description of LODI read [4], [37].

2.3.6 Compressible Flows

Compressible flows are such flows for which the density is not constant. Therefore, there is a clear coupling between the continuity equation and the momentum equation as the term $\nabla \cdot (\rho \mathbf{v})$, which determines the expansion in a system, is no longer zero. In aerodynamics flows are often considered incompressible for low speed flows, and compressible for high speed flows. Compression shocks can be present in such flows, which leads to the need for the discretized equations to be able to handle discontinuities to maintain monotinicity. Introducing combustion also leads to compressible flow. These factors increase the complexity of the flow, and therefore the equations are also more complex. There are an increased number of nonlinear

mechanisms and more unknowns. Furthermore, in compressible LES the cascading of eddies do not necessarily have to go one direction. They can also introduce energy transfer from a small time-scale to a larger time-scale eddy. [8], [42]

Since LES is used, a subgrid-scale is filtered out using a low-pass filter. This filter is based on the convolution product between the filter and the space-time variable. The filter is based on the spatial cutoff length Δ which is connected to the cutoff wave number k_c, as well as the cutoff time τ_c which is connected to the cutoff frequency ω_c. A few examples of filters is the Box filter, Gaussian filter and Sharp cutoff filter. [8], [42]

2.3.7 Governing Equations for Reacting Compressible Flow

The governing equations are generally expressed in Einstein summation convention or in tensor form. In this master's thesis the transport equations will be presented in tensor form.

For compressible, reacting flows neglecting radiative heat transfer, there are several transport equations; continuity for mass conservation, species mass fraction for each specie to conserve the elements present, conservation of momentum, and the energy transport equation to conserve energy.

Continuity

The continuity transport equation for turbulent combustion is

$$\frac{\partial \rho}{\partial t} + \nabla \cdot (\rho \mathbf{v}) = 0, \tag{2.35}$$

where ρ is the density, t is the time, $\mathbf{v}$ is the three-dimensional velocity vector. The temporal term is $\frac{\partial \rho}{\partial t}$ and the convective term is $\nabla \cdot (\rho \mathbf{v})$ which explains the spatial dilation (expansion or compression). [4]

Species

The species mass-fraction transport equation describing which mass fraction of each specie exists in a location at a specific time is described by

$$\frac{\partial \rho Y_k}{\partial t} + \nabla \cdot (\rho \mathbf{v} Y_k) = -\nabla \cdot (\mathbf{V}_k Y_k) + \dot{\omega}_k, \quad for \;\; k = 1, N, \tag{2.36}$$

where Y_k is the mass fraction for species k (m_k/M, where m_k is the mass of the species k, and M is the total mass), $\mathbf{V}_k$ is the diffusion velocity vector for species k, and $\dot{\omega}_k$ is the reaction rate for species k. [4]

Momentum

The momentum transport equation for turbulent combustion is

$$\frac{\partial \rho \mathbf{v}}{\partial t} + \nabla \cdot (\rho \mathbf{v} \otimes \mathbf{v}) = -\nabla p + \nabla \cdot \underline{\mathbf{S}}, \tag{2.37}$$

where p is the pressure, $\nabla \cdot (\rho \mathbf{v} \otimes \mathbf{v})$ is the non-linear advection term and $\underline{\mathbf{S}}$ is the shear-stress tensor. [4]

Energy

The energy transport equation for turbulent combustion is usually expressed in terms of the transport of specific enthalpy

$$\frac{\partial \rho h_s}{\partial t} + \nabla \cdot (\rho \mathbf{v} h_s) = \dot{\omega}_T + \frac{Dp}{Dt} + \nabla(\lambda \nabla T) - \nabla \cdot \left(\sum_{k=1}^{N} \mathbf{V}_k Y_k h_{s,k} \right) + \underline{\mathbf{S}} \nabla \mathbf{v}, \tag{2.38}$$

where h_s is the specific enthalpy, and $h_{s,k}$ is the specific enthalpy for species k, λ is the heat transfer coefficient, and T is the temperature. [4]

Acoustics in Reacting Flow

An expression for the acoustic transport equation for reacting flows can be derived by using the continuity-, momentum-, and energy transport equations together with the perfect gas law and a few other tricks. The resulting expression shows the transport equation for $ln(p)$

$$\frac{1}{\gamma}\frac{Dln(p)}{Dt}+\nabla\cdot\mathbf{v}=\frac{1}{\rho C_pT}\left[\dot{\omega}_T^{'}+\underline{\mathbf{S}}:\nabla\mathbf{v}-\left(\rho\sum_{k=1}^{N}C_{p,k}Y_k\mathbf{V}_k\right)\cdot\nabla T\right]+\frac{1}{R}\frac{DR}{Dt}, \quad (2.39)$$

where C_p and $C_{p,k}$ are the specific heat capacity coefficients where the indices k is for the specific specie.. [4]

The momentum equation can also be expressed as a function of $ln(p)$

$$\frac{D\mathbf{v}}{Dt}+\frac{c_0^2}{\gamma}\nabla ln(p)=\frac{1}{\rho}\nabla\cdot\underline{\mathbf{S}}. \quad (2.40)$$

[4] The material derivative of equation 2.39 from the divergence of equation 2.40 resulting in the wave equation for $ln(p)$

$$\begin{aligned}\nabla\cdot\left(\frac{c_0^2}{\gamma}\nabla ln(p)\right)-\frac{D}{Dt}\left(\frac{1}{\gamma}\frac{Dln(p)}{Dt}\right)&=\nabla\cdot(\frac{1}{\rho}\nabla\cdot\underline{\mathbf{S}})\\ -\frac{D}{Dt}\left[\frac{1}{\rho C_pT}\left(\dot{\omega}_T^{'}+\underline{\mathbf{S}}:\nabla\mathbf{v}-\left(\rho\sum_{k=1}^{N}C_{p,k}Y_k\mathbf{V}_k\right)\cdot\nabla T\right)\right]&\\ -\frac{D}{Dt}\left[\frac{Dln(R)}{Dt}\right]-\nabla\mathbf{v}:\nabla\mathbf{v}.&\end{aligned} \quad (2.41)$$

[4]

2.3.8 Constitutive Equations

When dealing with a system of equations, the number of unknown variables in the system must be matched with a same number of equations. Since the closure problem is often faced in numerics, constitutive equations are necessary. These are

a part of the foundation of the assumptions made when solving a problem. [8]

Ideal Gas Law

One of these constitutive equations commonly used in combustion is the ideal gas law. This law simply states that the quantities; pressure is linearly dependent on the product between temperature and density

$$\frac{p}{\rho} = RT. \tag{2.42}$$

[4]

Species sum is equal to 1

Another constitutive equation, which is very intuitive to use, is the one stating that if we have divide a normalized mass into different parts representing the different species present in a control volume, then the sum of all the mass fractions of these species must still equal the normalized mass. This is represented by a summation of the species mass fractions

$$\sum_{k=1}^{N} Y_k = 1, \tag{2.43}$$

where the summation goes from 1 to N which leads to an over-determined system of equations. This leads to the need to rewrite this constitutive equation

$$Y_N = 1 - \sum_{k=1}^{N-1} Y_k, \tag{2.44}$$

making the last specie be the remainder of the mass in the system which is unaccounted for. [4] Thus the species mass fraction from 1 through to $N-1$ are implicitly determined, while the mass fraction for specie N is explicitly determined.

Fick's Law

Fick's law is an empirical equation to describe the diffusion of a certain specie. This is described by

$$\mathbf{V}_k Y_k = -D_k \nabla Y_k, \tag{2.45}$$

where V_k is the diffusion velocity vector for species k, and D_k is the diffusion coefficient for species k. [4]

3 Numerics

3.1 Computational Fluid Dynamics

CFD is a tool commonly used to analyze fluid flow, heat transfer, and different phenomenon which can arise, such as chemical reactions. This technique has been introduced and widely used in the design of industrial products and processes due to the reduced cost in comparison to its experimental counter-part. There are several different methods for simplifying the reality to create a cost-efficient case to simulate. [8], [42]

The three most common methods utilized are RANS, LES, and DNS. RANS averages the NSE, removing the temporal fluctuating components. Therefore, it is not suitable for an unsteady simulation such as a bluff-body stabilized flame where the focus is to study thermoacoustics. DNS is expensive and currently mostly used in combination with RANS and/or LES, or for simple geometries and reaction mechanisms [8]. To be able to simulate a more detailed domain with an advanced reaction mechanism, LES is used in this master's thesis to capture the unsteady behaviour of the flow accurately in order to qualitatively capture the thermoacoustic instability. [4]

3.1.1 LES of Combustion Instabilities

As mentioned in literature such as by Poinsot and Veynante [4], to predict combustion instabilities, a method that can capture naturally unsteady flow is necessary. LES has this possibility, and is therefore a viable tool to use. However, it is still difficult to accurately predict such flow and capture the combustion instabilities correctly. A few key points that should be followed were mentioned by them and are listed below:

- Appropriate models for the flow and flow/chemistry interactions are necessary. [4]
- The implemented code to these models must work for complex geometries. However, this leads to unstructured grids which require more elaborate discretization schemes. [4]
- The boundary conditions need to be properly chosen and implemented to handle the transmission and reflections of acoustic waves. This leads to the need to test different impedances at the inlets and outlets to validate the simulation. [4]
- LES remains an expensive method, and thus limiting the domain is necessary, resulting in even more importance put on the boundary conditions. [4]
- Numerical waves can persist if the initial field is too harsh, thus the flow needs to be eased into the necessary conditions to properly capture the acoustics. [4]

3.1.2 Courant Number and stepping in time

Transient cases in CFD can become unstable and crash if the time-step is too large for a single cell to handle the convection of mass, species, momentum and energy. Since the velocities for which these cells convect the mentioned variables change, a fixed time-step is not favorable. A condition to decide whether the simulation will remain stable is the so-called Courant number. It takes the convection speed, magnitude of the time-step and how large the spatial step is into account. The Courant number is defined as

$$C = u\frac{\Delta t}{\Delta x}, \tag{3.1}$$

where u is the speed of convection, t is the time, and x is the spatial direction. This is applicable in all direction, thus for y- and z-directions, the speed of convection needs to be chosen to be the convection in the respective directions. [8], [43]

3.1.3 LES

LES resolves a certain amount of the actual turbulence and uses a turbulence model to resolve the rest. The minimum resolved turbulent kinetic energy is generally said to be 80 %. LES is the low-pass filtered DNS. Two examples of such spatial filters are box-filter's or Gaussian-filter's. The resolved turbulent kinetic energy is decided by the desired mesh size, and thus all frequencies are not captured due to limited mesh size will be filtered out. This results in the need of a model to capture the turbulent kinetic energy which was removed by the filter. If finite volume method is used, the conservative nature of the method will conserve the energy removed in the filtering. However, the schemes used need to be analysed before to ensure the simulation doesn't explode. [8], [44]

3.1.4 Subgrid-Scale Modeling

The turbulence model used to capture the filtered turbulent kinetic energy is the Dynamics Smagorinsky model. This model derives from the static Smagorinsky model which in turn derives from the RANS turbulence model, $k - \varepsilon$. RANS $k - \varepsilon$ model transports both the turbulent kinetic energy k, and the turbulent/eddy dissipation rate ε. Static Smagorinsky model transports the turbulent kinetic energy k, and uses a relationship between the turbulent kinetic energy and the turbulent dissipation rate ε. This is defined as

$$\nu_r = (C_{SGS}\Delta)^2 \underline{\bar{\mathbf{S}}}, \tag{3.2}$$

where ν_r is the eddy viscosity based on the residual motions, C_{SGS} is the Smagorinsky constant, and $\underline{\bar{\mathbf{S}}}$ is the filtered rate of strain tensor. [8], [44]

The dynamic Smagorinsky model allows the Smagorinsky constant, C_{SGS} to vary in time and space to match the flow-field. A test filter is run to calculate the constant at each time-step. It is important to note that the test filter's width needs to be greater than the grid filter. [45]

3.1.5 Combustion Modeling

There are different combustion models, such as the Flamelet model which assumes the chemistry time-scale is smaller than the Kolmogorov time-scale. Another model is the Eddy Dissipation Concept (EDC), which is based on the reaction sheets and eddies occupying a certain space in a control volume. Similarly to the eddy cascade, these control volumes cascade, which can be seen in figure 3.1. [8]

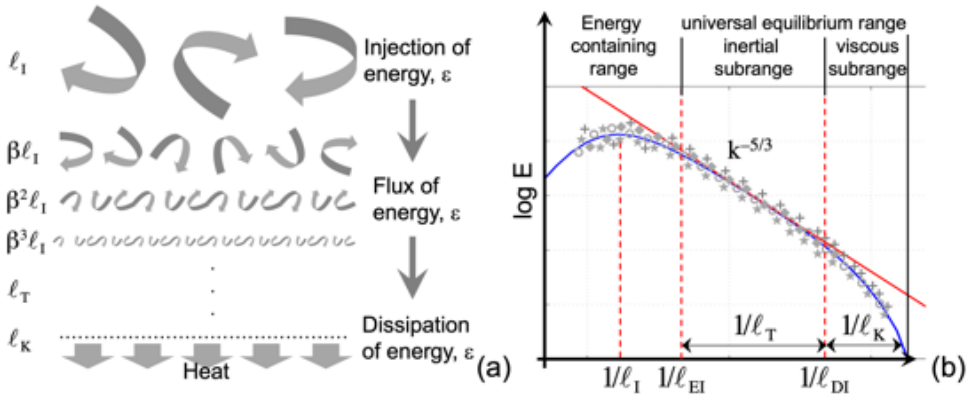

Figure 3.1 – An illustration of the cascade which the reaction sheets and eddies share in the EDC. This figure was obtained from the primary supervisor, Christer Fureby.

This leads to a control volume with both eddies and reaction sheets which affect each other based on the time-scales. The chemistry and turbulence time-scales form two non-dimensional numbers, Damköhler (Da) number and Karlowitz (Ka) number:

$$Ka = \frac{\tau_c}{\tau_K}, Da = \frac{\tau_I}{\tau_c}$$

where the chemistry timescale is defined as $\tau_c = \delta_u / S_L$, and the integral time scale $\tau_I = \lambda_I / v^{'}$, and lastly the Kolmogorov time scale $\tau_K = (\nu/\varepsilon)^{1/2}$. The different

timescales variables are as follows, δ_u is the laminar flame thickness ($\approx \nu/S_L$), and S_L is the laminar flame speed, λ_I is the integral length scale which is approximately the turbulent length scale, $v^{'}$ is the turbulence intensity, and ν is the molecular viscosity [8]. The Turbulence-chemistry interactions can be analyzed in the so-called Borghidiagram which can be seen in figure 3.2.

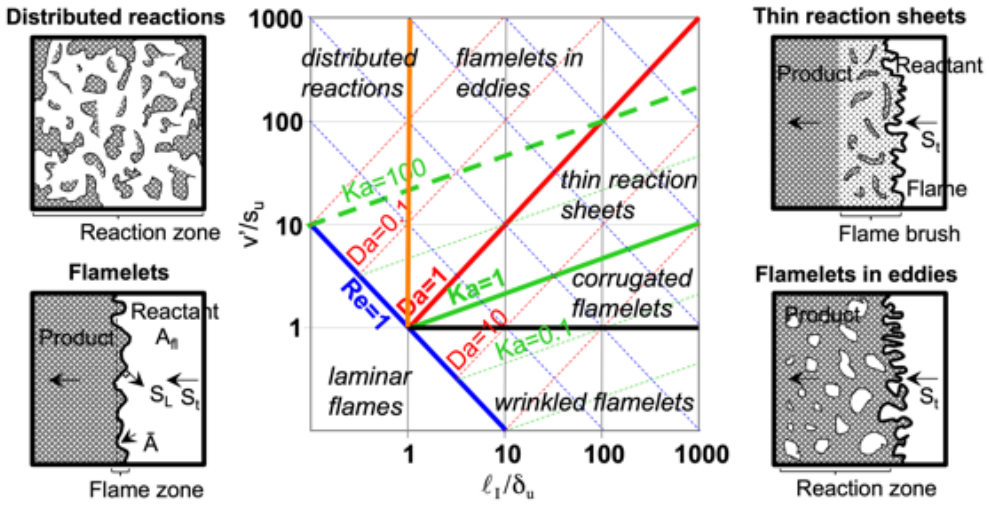

Figure 3.2 – How the Karlowitz and Damköhler numbers affect the flame dynamics which are signified by distributed reactions, wrinkled flamelets, flamelets in eddies, corrugated flamelets and thin reaction sheets. This figure was obtained from the primary supervisor, Christer Fureby.

3.1.6 Errors and Challenges

Numerical waves are explained well by Baritaud, Baum, Poinsot and Veynante in [37] and [4]. These waves are a consequence of numerical inaccuracies, and their development to an actual physical wave, is a consequence of too little numerical damping. Therefore, these waves cause increasing difficulties when performing DNS instead of RANS where artificial damping (turbulent/eddy viscosity) is implemented. For LES the artificial damping is often very low and causes problems similarly to

DNS. To reduce these waves, as much of the energy needs to be resolved, such as using fine meshes, and small time-steps to maintain a reasonable Courant number. The case set-up needs to be accurately set up as well, in the form of adequate boundary conditions. Another issue is imposing a too harsh initial internal field. If the field is not adequately transitioned to a reasonable internal field, the production of significant numerical waves can persist in the simulation indefinitely and be a part of the converged "physical" solution. Therefore, the person setting up such a case, need to do so with great care.

The Computational Cost increases greatly the closer the simulation is to reality. LES and DNS require high resolution, such that the numerical dissipation is as low as possible. Fine meshes and small time-steps are thus necessary since the spatial step is decreased while the convection speed is maintained (see equation 3.1). The computational cost is said to increase cubically for each doubled Reynolds number. Furthermore, the actual reactions can consist of several thousands of reaction mechanisms. However, each mechanism makes the simulation more complex, as well as each extra species introduces a new equation to be solved.

Reaction Mechanisms

A single-component fuel such as n-dodecane is present in diesel fuel and has been found useful to predict flame dynamics at a lower cost than simulations using multicomponent fuels such as diesel. A detailed skeletal reaction mechanism for n-dodecane was developed at the University of Southern California by You et al. [46] to act as a surrogate for diesel fuel. Some high T-pyrolysis reactions were removed by Tong et al. [13] creating the SK54 reaction mechanism. It consists of 54 species and 269 reactions which were carefully chosen to predict the ignition delay at low temperature conditions which was previously not as well predicted. However, previous mechanisms had a decent prediction of ignition delay at high temperature conditions. Since each specie's mass fraction needs to be transported, it includes

an extra transport equation to be solved. Comparing SK54 with another detailed skeletal reaction mechanism using n-alkanes, n-octane and n-hexadecane, developed by Westbrook et al. [47], consists of 2775 species and 11173 reactions. Such a detailed reaction mechanism needs to be reduced to be computationally plausible for combustion systems. [13]

The SK54 mechanism was tailored by trying to include more low-temperature reaction mechanisms to be able to more accurately predict the ignition delay at such temperatures. These simulations and experiments were done for spray injections which include high pressure levels between 10 - 50 bar. The ignition delay is plotted as a function of $1000/T\,(K^{-1})$ in a semi-log plot where the ignition delay is value with the logarithmic axis. An example of such a plot adapted from Yao et al. study can be seen in figure 3.3. [13]

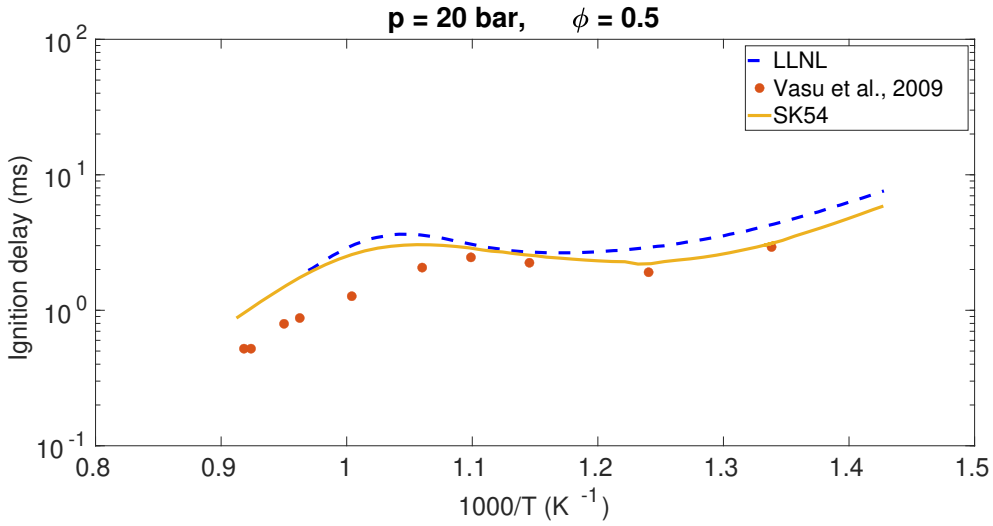

Figure 3.3 – The ignition delay plotted as a function of $1000/K$. Illustrating how the reaction mechanism predicts the ignition delay in comparison to experiments. Adapted from Tong et al. [13]

3.2 OpenFOAM

3.2.1 PIMPLE Algorithm

When simulating different flows, there are two ways to decide how to solve the pressure and velocity. Either they are solved simultaneously (coupled solvers), or

separately in an iterative algorithm (segregated solvers). The latter requires the decoupling of the pressure and velocity, leading to an initial prediction of a certain variable (pressure for pressure-based solvers, or density for density-based solvers), solving the momentum equation, correcting the pressure or density, and then solving the momentum and the rest of the transport equations. The decoupling of the pressure and velocity has found to impact the speed of convergence and is highly used in CFD simulations. [8], [48]

The PIMPLE algorithm is a combination of the SIMPLE (Semi-Implicit-Method-for-Pressure-Linked-Equations) and PISO (Pressure-Implicit-Splitting-of-Operators) algorithms. SIMPLE solves a steady state problem, while PISO is more favourable for transient problems. These procedures can be seen in appendix A, in figures A.1 and A.2. Transient SIMPLE algorithm iterates through the same steady-flow SIMPLE algorithm but with an external loop for the time-propagation. The PISO algorithm solves is similar to SIMPLE, however it includes a re-correction, thus each iterations converges slightly better. [8], [48], [49]

The PISO algorithm introduces errors which can be reduced with more pressure correctors. The PISO algorithm has also been found to accumulate minimum magnitude of errors if the Courant number is close to unity. However, for high-frequency flows, the Courant numbers impact outweighs that of the PISO algorithm. Thus it is more favourable to have the optimal Courant number, rather than one close to unity. [43]

3.2.2 Boundary Conditions

BC's are very important when setting up your case. They decide whether or not your solution will be physically correct. However, even if it may be physically correct with the experimental set-up, it might not always be correct to use the same BC for simulation set-up. The experiments do not have numerical dissipation which affect the flow acoustics and heat oscillations, but rather, measurement equipment that

have different tolerances, and issues picking what species to measure temperature by, due to difficulty in tracking it.

WaveTransmissive BC

The waveTransmissive BC is a RBC, meaning it is a mix between the DBC and NBC. It is implemented in OpenFOAM using Linear One-Dimensional Inviscid which is commonly referred to as Euler flow. This implies that the only transmitted waves are the ones which are normal to the outlet-patch's cells. The goal of using such a boundary condition is to manage the amount of reflected waves. The BC has several inputs; the field it is imposed on, e.g. pressure 'p', ratio of specific heats γ, the volumetric flux field ϕ or a mass flux field which will be divided by the density field ρ, the compressibility field, ψ which is defined as the derivative of ρ with respect to p, the distance to the far-field condition in meters l_∞, the far-field value ϕ_∞, and lastly the value at the neighbouring cell to the outlet patch. [41]

The effect the waveTransmissive BC can be analysed in

$$L_1 = K(p - p_\infty), \tag{3.3}$$

where $K = (u + c)/l_\infty$, L_1 is the pressure which will adjust the pressure at the boundary according to LODI theory, and p, p_∞ are the pressures at the neighbouring cell to the outlet, and the far-field pressure, respectively. [4], [41]

4 Implementation

In this chapter the base case setup will be presented, including the system description; dimensions of the system and boundary conditions as well as the meshing. After the presentation of the system, there will be an introduction to the numerical implementation, including the different schemes used for the terms in the governing equations. Next, the different cases tested are presented, such as the different boundary conditions and which equivalence ratios are tested. Lastly, the measurement locations are introduced as well as the choice of how to process the data obtained.

4.1 Case Setup

The case setup includes a rectilinear channel with an equilateral triangular bluff-body. The dimensions of the rectilinear channel is 1.56x0.12x0.08 m^3 (length x height x width). The width of the channel is approximately half of the experimental setup to minimize the computational cost. Instead of simulating the entire domain, a cyclic boundary condition is used on the side walls to compensate. Note that this means the wall effects on the sides are neglected. If one were to draw the rectilinear channel using two points (x_{min}, y_{min}, z_{min}) and (x_{max}, y_{max}, z_{max}), it would be presented as (-0.56, 0, 0) and (1, 0.12, 0.08) in meters. The three corner points on the triangular bluff-body are located at (0.27, 0.06, 0), (0.31, 0.08, 0) and (0.31, 0.04, 0). This surface is extruded in the z-direction. This can be seen in figure 4.1.

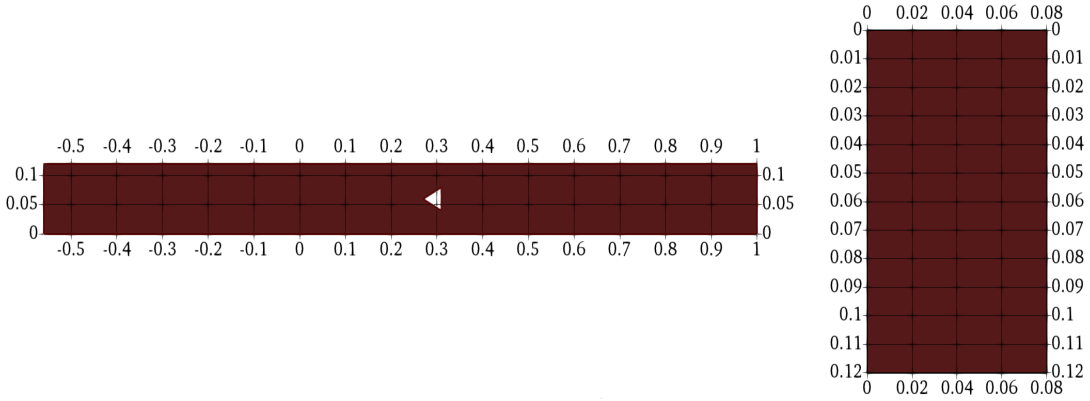

Figure 4.1 – An illustration of the case dimensions. The top figure being the XY-plane, and bottom figure the YZ-plane.

The most common modes which will be present are the first and third-longitudinal mode in the combustion chamber (1L-CC, 3L-CC), as well as the first- and third-longitudinal mode from the bluff-body to the outlet (1L-BB, 3L-BB). These are illustrated in figure 4.2.

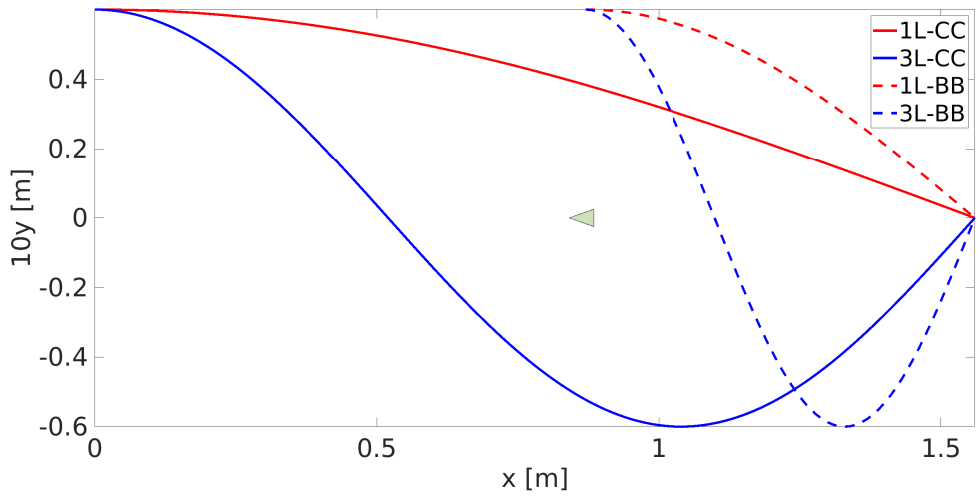

Figure 4.2 – An illustration of the pressure-waves in the combustors/ afterburners domain. The 1L-CC (red), 3L-CC (blue) illustrated with solid lines. The 1L-BB (red), 3L-BB (blue) illustrated with dashed lines.

4.1.1 Boundary Conditions

The base case boundary conditions are set as presented in table 4.1 and figure 4.3.

Table 4.1 – The base case's boundary conditions

Boundary	**Condition**	
Inlet	p	zeroGradient.
	U	fixedValue uniform (34 0 0) m/s.
	T	fixedValue uniform 600 K
Outlet	p	waveTransmissive, gamma 1.3, fieldInf 101300 Pa, lInf 0.1 m.
	U	zeroGradient.
	T	zeroGradient.
Top Wall	p	zeroGradient.
	U	noSlip.
	T	fixedValue uniform 600 K.
Bottom Wall	p	zeroGradient.
	U	noSlip.
	T	fixedValue uniform 600 K.
Side Wall 1	p	cyclic (paired with Side Wall 2).
	U	cyclic (paired with Side Wall 2).
	T	cyclic (paired with Side Wall 2).
Side Wall 2	p	cyclic (paired with Side Wall 1).
	U	cyclic (paired with Side Wall 1).
	T	cyclic (paired with Side Wall 1).
Bluff-Body Walls	p	zeroGradient.
	U	noSlip.
	T	zeroGradient.

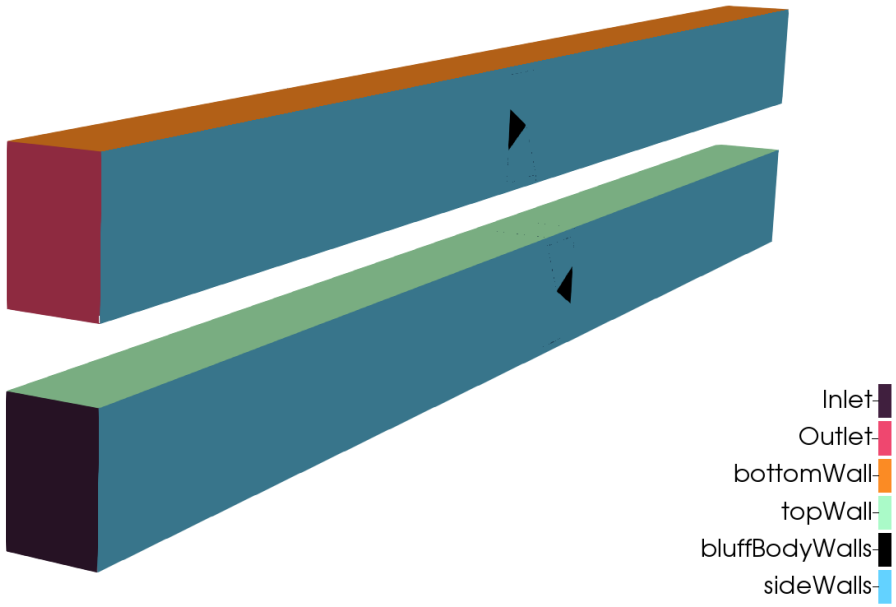

Figure 4.3 – An illustration of where the different boundaries are located in the system-domain. Inlet (dark-red), Outlet (red), bottomWall (orange), topWall (light-green), bluff-BodyWalls (black), and sideWalls (grey-blue)

4.1.2 Initial Conditions

The initial field was generated by the supervisor and every subsequent case was run starting from a previous case to save computational cost. In order to minimize the numerical artifacts when changing the equivalence ratios, the case was first turned cold with the new equivalence ratio, two flow-through times to remove possible contamination, and to create a new internal field, followed by the re-ignition of the engine (turning the reactions back on).

When changing the outlet boundary conditions, the case was simply continued with the new boundary conditions and simulated until the transients were removed, and later continued to collect data/results.

4.1.3 Mesh

The mesh was created directly in OpenFOAM using blockMeshDict. In this dictionary for the mesh, one specifies vertices which are later connected by blocks, and lastly the boundaries are defined on these blocks. The mesh used in this study was

not generated by the author, but provided by the supervisor.

When it comes to meshing to run a LES, the mesh needs to be fine enough to capture approximately 80% of the turbulent kinetic energy. Since the turbulent kinetic energy is greater in different regions than others, this requires some intuition. The bluff-body is an obstacle which will alter the flow and create a vortex break-down. Therefore, it is logical to refine the mesh downstream of the bluff-body. This is done using OpenFOAM's simpleGrading in blockMeshDict. This simply redistributes the cells in a given defined block by a defined gradient. The current mesh has 6819600 number of cells.

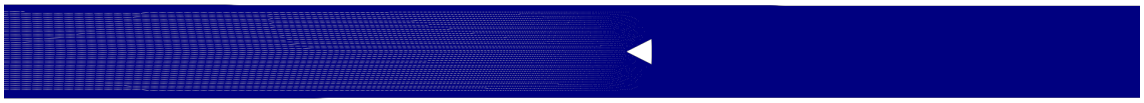

Figure 4.4 – The entire system-domain's mesh.

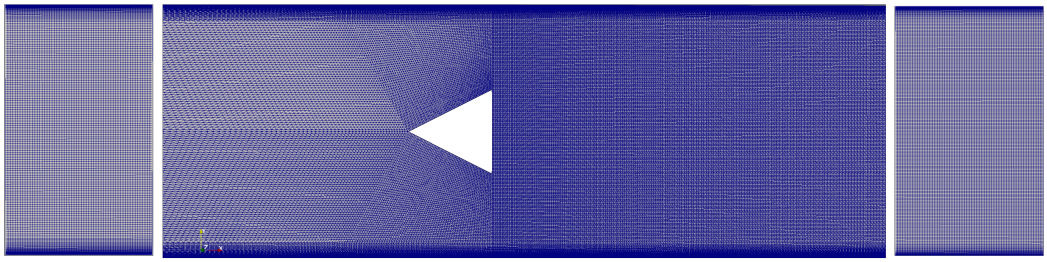

Figure 4.5 – Mesh seen from the inlet (YZ-plane), at the BB (XY-plane), and outlet (YZ-plane) from left to right.

4.1.4 Reaction Mechanism

The reaction mechanism used is the SK54 developed partly in University of Southern California (USC), and later optimized for low-temperature reactions by Tong, et al. [13]. This reaction mechanism consists of 54 species and 269 reactions.

n-dodecane consists of 12 carbon atoms and 26 hydrogen atoms. A simple global reaction mechanism can be seen below:

$$2C_{12}H_{26} + 37\phi(O_2 + \frac{79}{21}N_2) \longrightarrow 24CO_2 + 26H_2O + 37 \cdot \frac{79}{21}N_2,$$

where ϕ is the equivalence ratio, defined as $\phi = \frac{AFR}{AFR_{st}}$. AFR stands for air-to-fuel-ratio, and the index 'st' stands for stoichiometric. If $\phi = 1$, the global reaction mechanism is easily satisfied as above. However, if $\phi \neq 1$, the products will be greatly affected.

4.1.5 Simulation setup and assets

The simulation was, as previously mentioned, set up in OpenFOAM. The case was partly supplied by the supervisor. The author adjusted some BCs to perform the sensitivity analysis with the help of the supervisors. Since the required amount of data to analyse a complex phenomenon such as thermoacoustics is large, the method of extracting this data needed to be created. The supervisor had previously created probes which were sampled for each time-step which is roughly 2 μs. In addition to this, field averages were created in order to obtain the mean pressure and root-mean-squared pressures in order to analyze to perform the POD-analysis. Furthermore, weighted area integrates were created to swiftly gather the pressure (including mean pressure, and root-mean-squared pressure), velocity and temperature data for the measurement locations seen in the measurement subsection below in figure 4.6.

4.1.6 Discretization

The discretization schemes used vary depending on what type of term is investigated. A list of the discretizations used can be found below:

- Time - Euler Implicit $\phi^{t+1} = \frac{\phi^t - \phi^{t-1}}{\delta t}$.
- Gradients - cellLimited Gauss linear.
- Divergence - Gauss linear, Gauss Gamma.
- Laplacian - Gauss linear corrected.
- Interpolation - Linear.

The generic forms of these terms are $\frac{\partial \phi}{\partial t}$ for the temporal terms where ϕ is a generic variable, $\nabla\phi$ for the gradient terms, $\nabla \cdot \phi$ for the divergence terms, $\nabla^2\phi$ for the laplacian terms.

4.2 Different Cases

The master's thesis investigates five different cases. The first case includes n-dodecane with equivalence ratio 0.66 and waveTransmissive BC with $l_\infty = 0.1$ m. The second case uses the same equivalence ratio and waveTransmissive BC but with $l_\infty = 1.0$ m. Case 3 and 4 includes n-dodecane with equivalence ratio 0.87 and waveTransmissive BC with $l_\infty = 0.1$ m for case 3, and $l_\infty = 1.0$ m for case 4. Case 5 includes a comparison for equivalence ratio 0.66 where the outlet is set to fixedValue which is considered a reflective boundary. These are relisted in table 4.2

Table 4.2 – Different cases' set-up

Case	Equivalence ratio	BC
Case 1	0.66	waveTransmissive $l_\infty = 0.1$ m.
Case 2	0.66	waveTransmissive $l_\infty = 1.0$ m.
Case 3	0.87	waveTransmissive $l_\infty = 0.1$ m.
Case 4	0.87	waveTransmissive $l_\infty = 1.0$ m.
Case 5	0.66	fixedValue 101300 Pa.

4.2.1 Measurements

The different measurement locations include probes and integrated averages from different defined slices. These can be seen in figure 4.6, where the probe locations are all behind the bluff-body to observe the changes in temperature, velocity and pressure downstream and in the vertical direction. To compare with the experiment, two slices are taken at the back-pressure plate and bluff-body. Since the outlet boundary condition is difficult to determine in order to investigate thermoacoustic behaviour, data for the outlet has been collected.

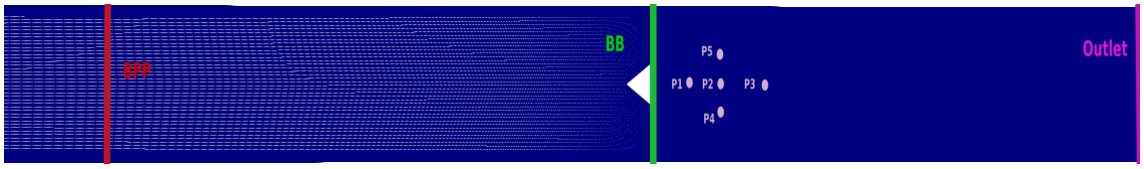

Figure 4.6 – A figure visualizing where the different measurements are located. The red line represents the back-pressure plate slice, the green line represents the bluff-body slice, the pink dots represent the five different probe locations, and lastly the purple line represents the outlet slice.

As mentioned in the background section, a minimum of two measurement points are necessary to capture the wave-length of a certain frequency. This creates a demanding sampling frequency for a system with high frequency excitation. KH frequency is expected to be at about 5 kHz, and thus the requirement is a minimum of 10 kHz sampling frequency. For higher resolution, 20 kHz frequency was chosen.

To minimize the amount of data stored in these extra data times, only the pressure, mean pressure, root-mean-squared pressure, velocity, temperature, formaldehyde, hydroxide, and aldehyde were stored.

4.2.2 Processing Data

To process data, POD will be used in conjunction with FFT in order to capture the excited frequencies, as well as the predominant POM to visualize which coherent structures dominate the pressure-field.

5 Result and Discussion

5.1 Outlet Boundary Sensitivity Analysis

In this section the different results obtained from changing the outlet's boundary condition will be presented in the order of Case 1 to Case 5.

Case 1 resulted in a very high pressure amplitude which can be seen in figure 5.1. These are much higher than the experimental study done by Paxton et al. [10]. It shows a pressure-wave amplitude of almost 7 kPa, whilst their study measured approximately 500 Pa. Furthermore, their study showed two almost equally excited frequencies, the 1L-CC and 3L-CC. In case 1, the 3L-CC mode was completely dominant. The reason for this increase was further studied by changing the distance for which we define the infinite field pressure.

Case 2 showed a great decrease in pressure-wave amplitude as well as only the 1L-CC being excited. The decrease in pressure-wave amplitude indicates that the distance set from the outlet to the infinite field has a damping effect on the system, similar to an extension of a channel/duct. However, the change in excited frequency indicates that the previously excited 3L-CC wave can no longer be self-sustained. This could be due to the change in outlet boundary condition leading to a change in the acoustic impedance. As stated in the background section, the impedance varies for different frequencies [4], [32]. Another reason could be that the mean values for the pressure and temperature change such that the ignition delay time is affected, resulting in a change in which frequency that becomes unstable (see figure 3.3). An increase in pressure generally decreases the ignition time delay, whilst an increase in temperature can have both effects [13].

Case 3 is expected to potentially have higher pressure-wave amplitude due to the possibility for more energy to be fed into the acoustic field. Furthermore, the increase in equivalence ratio should lead to an increase in temperature and thereby, an increase in speed of sound. This occured in the experiment by Paxton et al. [10]. Peculiarly this does not occur in the simulation. Instead the pressure-wave amplitude is slightly higher than that of case 2, but much lower than case 1. The reason for this is most likely due to the increase in temperature and thus speed of sound, leading to a shift in acoustic impedance for all possible resonance frequencies. More specifically, the frequencies naturally excited by the systems BB position, blockage ratio, combustion mechanics and inlet velocity, might have become dampened more than the temperature and speed of sound increase would help excite these frequencies.

Case 4 should lead to a lower pressure-wave amplitude if the increase in l_∞ follows a linear trend similar to the difference between case 1 and 2. However, this is not observed, instead the pressure-wave amplitude is slightly increased. This further indicates the possible dependence on outlet's input acoustic impedance which is a cotangent function. At this moment, it is not possible to say exactly what is the cause as this needs to be investigated further. This implies that the waveTransmissive BC somehow exhibits the same behaviour as a realistic outlet which has not been verified.

Another possible cause of this behaviour, is that the outlet causes the imaginary part of the wave-number's fluctuation to be close to zero for the 1L-CC mode, and negative for the 3L-CC. This would result in the energy fed by the heat release oscillation (which create spherical pressure-waves) to the velocity fields oscillations occurs such that their product is approximately zero (almost 90° out of phase) leading to a slightly excited 1L-CC, but a non-existant 3L-CC mode. This cause would concur with the stability domains derived by [4].

Case 5 is expected to reach extremely high pressure-wave amplitudes as a fixed

value (Dirichlet) boundary condition is known to be reflective [4], [32], [37]. This is observed, and the simulation had to be adjusted to remove the possibility of back-flow to be continued. This was done by introducing pressure-Inlet outlet velocity boundary condition which works as zero gradient for exiting flow, and imposes zero velocity for back-flow. The pressure-wave amplitude had not reached its statistically steady state, and the large pressure-wave amplitude leads to high velocities, decreasing the time-step needed which leads to a more expensive simulation. Therefore, this simulation was stopped before the limit-cycle was reached.

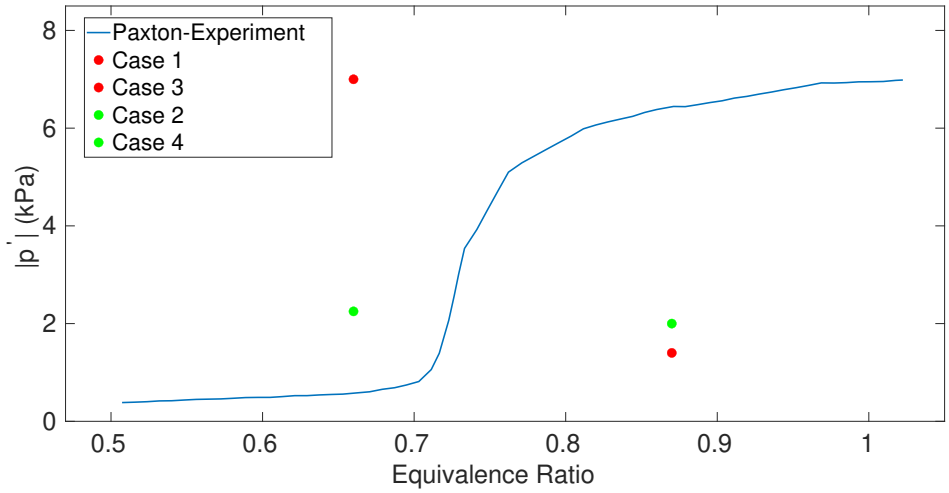

Figure 5.1 – An adaptation of the experimental results by Paxton et al. with some points for comparison acquired in the simulation. The red dots are the cases where the distance $l_\infty = 0.1$ m, and the green dots are the cases for which $l_\infty = 1.0$ m. [10]

5.1.1 Flame-Dynamics

The reacting flame-sheet consists of different intermediate and radical species. One of these radicals is formaldehyde. This makes formaldehyde a good specie to observe when visualising the flame-dynamics. Thus the following figures use the formaldehyde concentration to visualise the flame-dynamics.

The flame-dynamics in case 1 show extremely high pressure-fluctuations, with a pulsating behaviour which can be seen in figure 5.2. This pulsating behaviour is signified by the necking of the flame behind the bluff-body. The process begins by the increased inclination of the flame relative to the bluff-body's trailing edges.

Later, the growth of the two twin vortices due to the bluff-body's geometry (also present in cold case) creates a low-pressure zone [3]. The pressure-gradient from the recirculation zone to the wake increases as the necking proceeds and the upper and lower flame-sheets become increasingly close to each other. Lastly, the inclination of the flame relative to the bluff-body's trailing edges decreases, signifying the end of the periodic cycle.

Many dynamic phenomena are occuring simultaneously, as the vortices are discharged from the bluff-body in the last snapshot, but quickly dampened due to the high viscous diffusion caused by the burned gas' high temperature [3]. At the same time, combustion occurs which leads to gas expansion which pushes the flame-sheets towards all directions and reducing the vorticity fields magnitude. Due to the axial direction being the dominant flow-direction, this expansion is mostly towards the walls and outlet.

The first snapshot shows some asymmetric behaviour, which is most likely due to the presence of BVK instability [9]. This asymmetric behaviour does not seem to be dominant which is an indication that the ratio between the burned and unburned gas' is high (T_b/T_u) [27].

In comparison to the experiment by Paxton et al., the pulsating behaviour is greatly overestimated. In their experimental study, the pulsating behaviour is barely present. The behaviour seen in case 1 is more similar to their case with an equivalence ratio of 0.75. When discussing the difference between these results, it is important to remember that there are many assumptions in simulations, such as smooth surfaces and more. As seen in figure 2.4, the Strouhal frequency changes greatly if the Reynolds number is increased slightly above 10^5, which is not as dramatic as for the rough surface. However, figure 2.4 is for cylindical bluff-bodies and not triangular bluff-bodies.

As mentioned in the boundary sensitivity analysis, the outlet's boundary condition

is of great significance, which concurs with Poinsot and Veynante [4]. This may be what affects the differences observed between the simulations and their experimental study the most.

As mentioned in the acoustics section, the pressure anti-node characterises a compression at the crest, and a rarefaction at the trough. Due to the placement of the bluff-body, the pressure anti-node is located in its wake if the 3L-CC wave is excited. Since this is the case for case 1, it is likely that this is what causes this type of pulsating behaviour leading to the necking of the flame.

In the experiment by Paxton et al., this necking persists as the 3L-CC mode is excited enough. Since the 3L-CC mode is not the most excited mode throughout all of the cases, it can be seen as a superimposed frequency on the main pressure-wave, and thus this pulsating behaviour is clearly affected by the other modes as well.

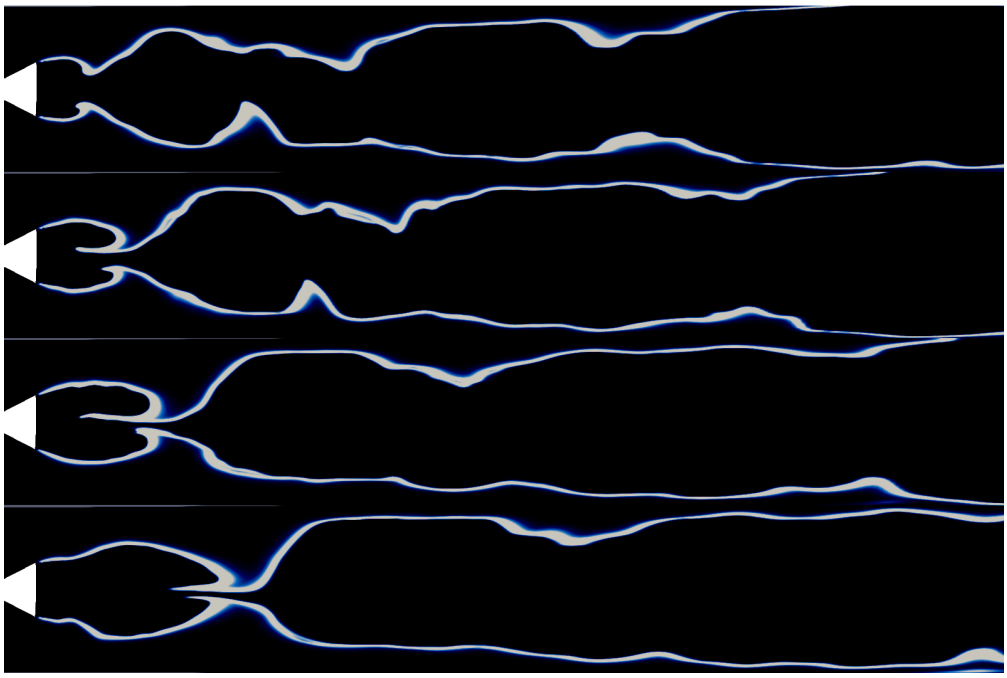

Figure 5.2 – An illustration of the flame-dynamics for case 1 using the concentration of formaldehyde. Four snapshots are used to capture an entire period of the flames oscillating behaviour.

In case 2, the flame-sheets dynamics are much milder as seen in figure 5.3. Note that the difference between case 1 and 2 is only at which length away from the outlet, the

infinite field is placed. The flame-sheet does not have a clear pulsating behaviour, and the behaviour is more asymmetric. Case 2 is more similar to the experiments equivalence ratio of 0.72, rather than 0.66, indicating that the system needs to be dampened further.

Due to the decrease in pressure-fluctuations, the decrease in pulsations magnitude is reasonable. The asymmetric behaviour is usually connected to the flame-temperature ratio as previously mentioned. The equivalence ratio for these two cases are the same, thus the potential heat release should not be changed. A reason for a slight change in the flame-temperature ratio could be due to the decrease in combustion efficiency, since the thermoacoustic instability is known to increase the combustion efficiency [4].

The behaviour seen in figure 5.3 is similar to that of the experiment by Paxton et al. The magnitude of the expansion due to the discharging of bluff-body generated vortices together with the combustion intensity is only slightly higher. This indicates that the distance to the infinite field for an equivalence ratio of 0.66 should be set to 1.0 m rather than 0.1 m as done in case 1.

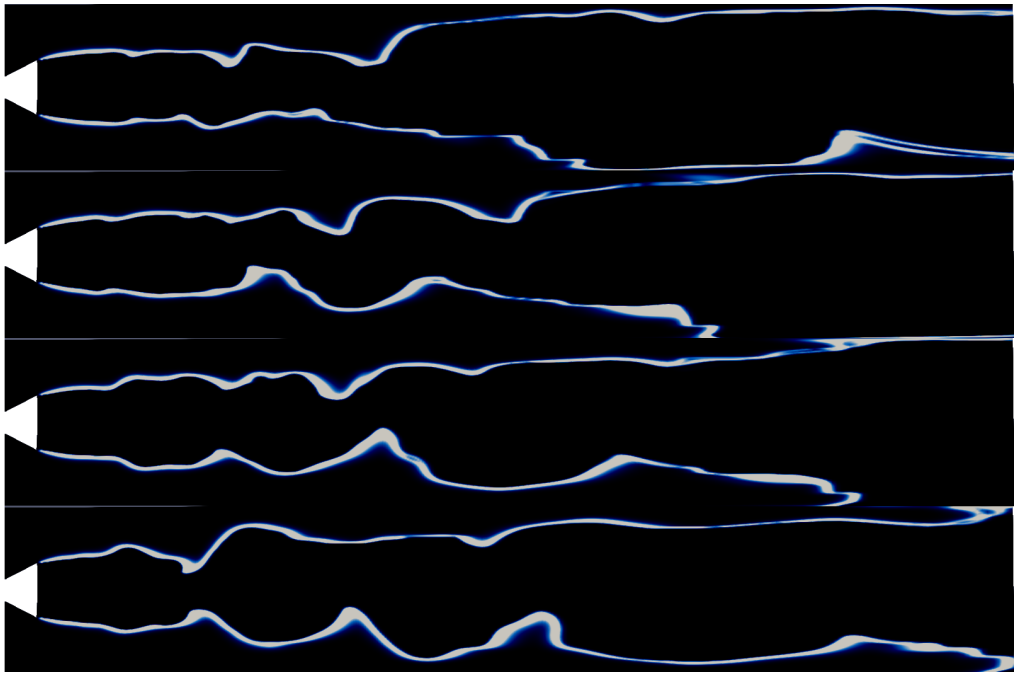

Figure 5.3 – An illustration of the flame-dynamics for case 2 using the concentration of formaldehyde. Four snapshots are used to capture an entire period of the flames oscillating behaviour.

If the equivalence ratio is changed to 0.87 as done in case 3 and 4, the thermoacoustic instability is expected to increase as it does in the experiment by Paxton et al. For case 3 with the distance to the infinite field set to 0.1 m, the snapshots in figure 5.4 show significantly lower pulsating behaviour than that of case 1 when the reverse is expected. This indicates that when simulating and trying to capture the thermoacoustic instability in a system, there are other important parameters than just the equivalence ratio as in the experiments. The temperature increases as the equivalence ratio approaches stoichiometric combustion, which naturally increases the resonant frequency requiring a different specified distance if the position of the pressure node is to be accurately predicted.

The concentration of formaldehyde seems to have some sharp spatial gradients in the flame-sheet. These are most likely due to numerical artifacts, i.e. mesh quality over the flame. In these sharp spatial gradients, the flame would only have one cell which can cause large numerical diffusion causing the flame to appear smeared.

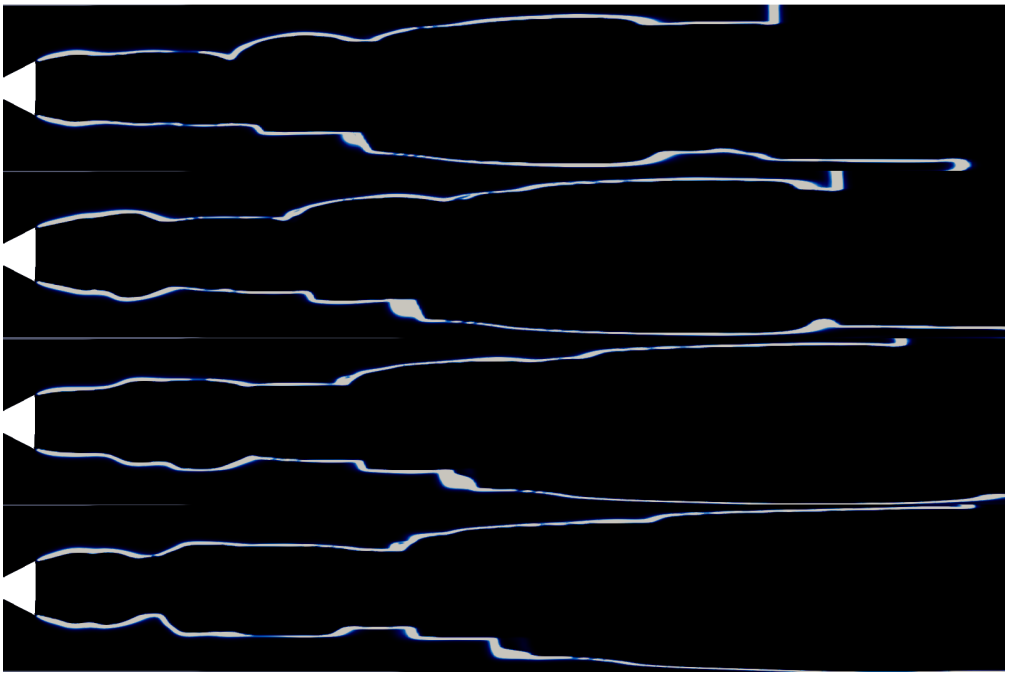

Figure 5.4 – An illustration of the flame-dynamics for case 3 using the concentration of formaldehyde. Four snapshots are used to capture an entire period of the flames oscillating behaviour.

In case 4, the equivalence ratio remains at 0.87 but the specified distance to the infinite field is increased to 1.0 m, similar to case 2. If the result is to be similar to the changes occurring between case 1 and 2, the pressure fluctuations should decrease, and lead to an even lesser pulsating behaviour. However, in this case the pressure fluctuations increase and the pulsating behaviour increases slightly. Analysing figure 5.5, a larger expansion can be observed at the trailing edges of the bluff-body. This indicates that the specified distance does not simply dampen the pressure fluctuations in the system, but rather it follows some non-linear behaviour. A potential reason for this is that the input acoustic impedance could have a non-linear periodicity as that of the co-tangent curves shown in Appendix B, in figures B.1 and B.2. Note that the surf-plots of the input acoustic impedance are co-tangent-curves frequency are a function of both the length of the channel, and the speed of sound. Thus, there is a slight change which occurs and can be easily calculated, due to the increase in temperature when approaching stoichiometric combustion.

Another possibility for the non-linear behaviour, is if the combustion is dampened

so the acoustic oscillations at the frequency represented by the wave-number's mean is increased. This is mentioned by [4]. The given modes are stable under certain circumstances which depend on the geometry and speed of sound.

Similarly to what was observed in case 3, the sharp spatial gradients of the formaldehydes concentration could indicate an insufficient mesh resolution, or possibly due to other numerical issues.

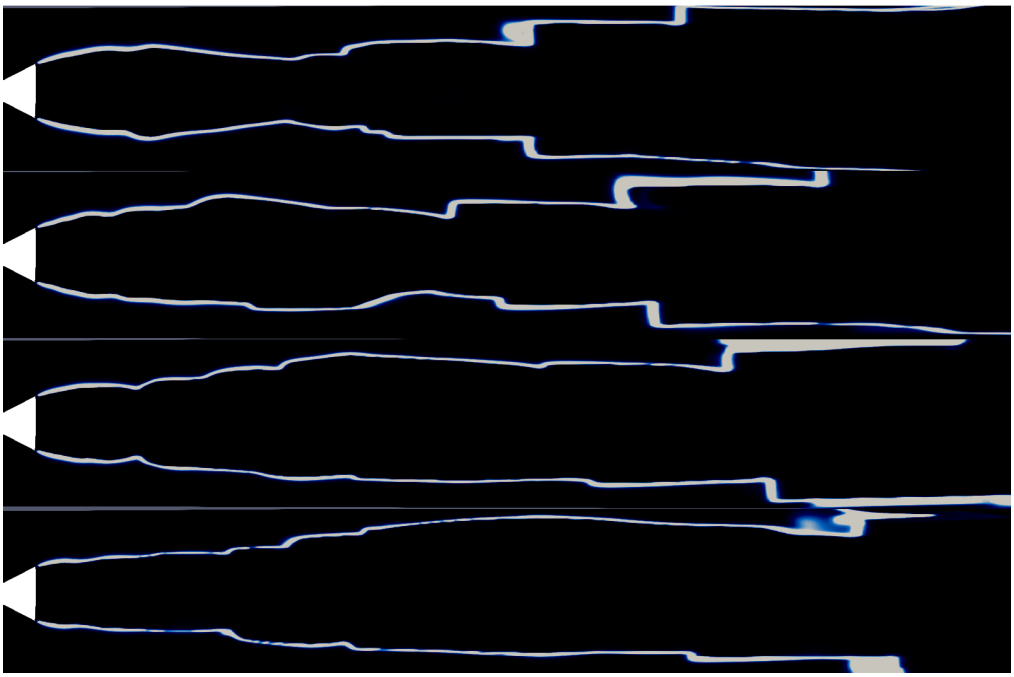

Figure 5.5 – An illustration of the flame-dynamics for case 4 using the concentration of formaldehyde. Four snapshots are used to capture an entire period of the flames oscillating behaviour.

Instead of changing the specified distance to be further away from the outlet, it is set to be exactly at the outlet causing the pulsating behaviour to intensify. This is due to the reflective nature of a fixed value BC [4], [37]. Case 5 never reached a limit-cycle due to the increasing computational cost as the pressure and velocity increased. The intense pulsating behaviour can be seen in figure 5.6. The necking almost pinches the flame off, which occurs in some snapshots, however it is recovered when the vortices are discharged, and the gas expands accelerating to merge with the other burned gases and flame-sheets. It is clear that the fixed value boundary condition used in this study is not suitable when analysing thermoacoustic instability

for a jump into a large cavity at the outlet.

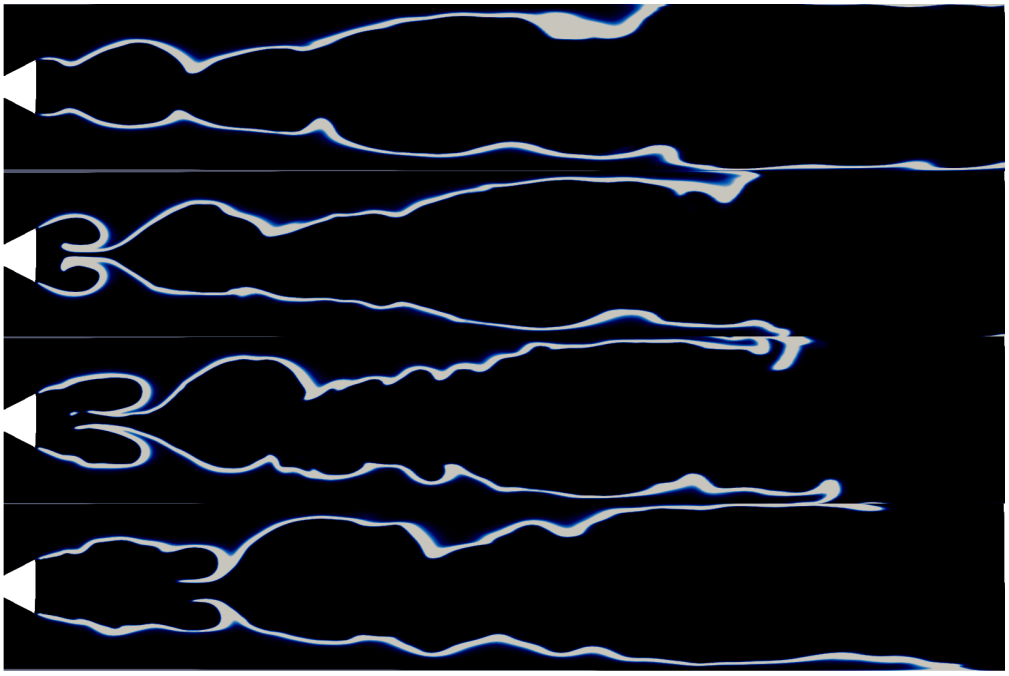

Figure 5.6 – An illustration of the flame-dynamics for case 5 using the concentration of formaldehyde. Four snapshots are used to capture an entire period of the flames oscillating behaviour.

From these results on the boundary condition analysis, case 2 and 4 will be continued since they concurred the most with the experimental study done by Paxton et al. This can be seen in figure 5.1.

5.2 Fast Fourier Transform

In this section the results from analysis the pressure fluctuations at BPP and BB, will be presented. These will be compared to the experimental results acquired by Paxton et al. [10]

In figure 5.7, case 2's FFT at the bluff-body can be seen. The first graph is the FFT where the y-axis is the pressure-fluctuations amplitude in Pa, whereas the second graph is the pressure-fluctuations in dB and compared with the experimental results. For case 2, the 1L-CC, 1L-BB, 3L-CC, were observed to be 102 Hz, 215 Hz, and

276 Hz. The 1L-CC and 3L-CC can be compared to the frequencies observed in the experiment which were 91 Hz, and 273 Hz. [10]

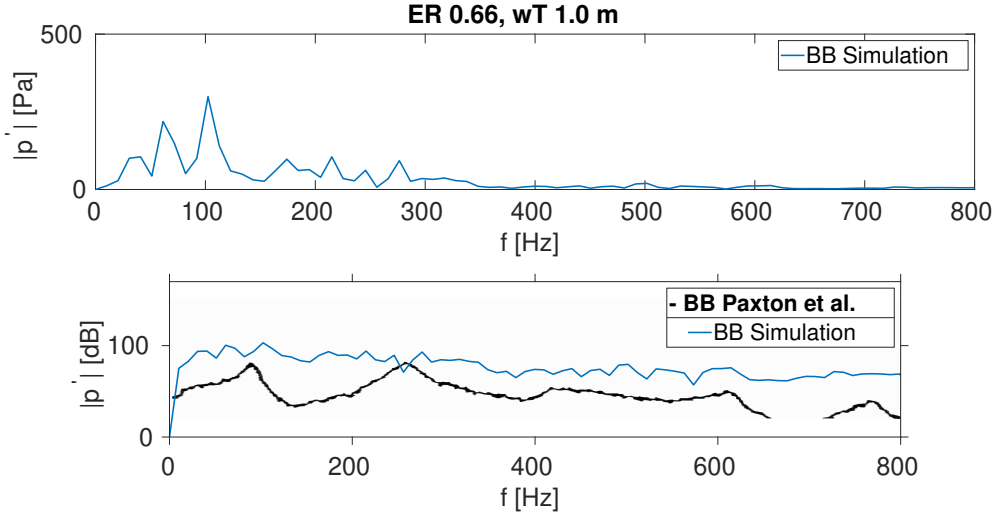

Figure 5.7 – A FFT of the pressure-fluctuations for case 2 at the bluff-body. The top figure is a linear-linear plot, whilst the bottom figure is a log-linear plot with decibels as the y-axis. This is compared with the experiment by Paxton et al. [10] which is represented by the black line.

The FFT at the bluff-body can be seen in figure 5.8 for case 4. The frequencies observed in case 4 were 96 Hz, 200 Hz, and 258 Hz, respectively. The frequencies the experiment by [10] observed were 119 Hz, 240 Hz, 357 Hz and 430 Hz. The highest of these frequencies was not discussed in their analysis. The first three correspond to the 1L-CC, 1L-BB and 3L-CC. The simulations under-predict these frequencies which is likely due to the outlet BC as it is possible the time delay between heat release and velocity perturbations cause this. This implies that the energy stored to activate the reaction does not feed the energy back to the acoustic-field at the right time. This would lead to these modes not being as excited. The explanation for this is formulated in the section for $n - \tau$ formulation which was presented in the background chapter [4].

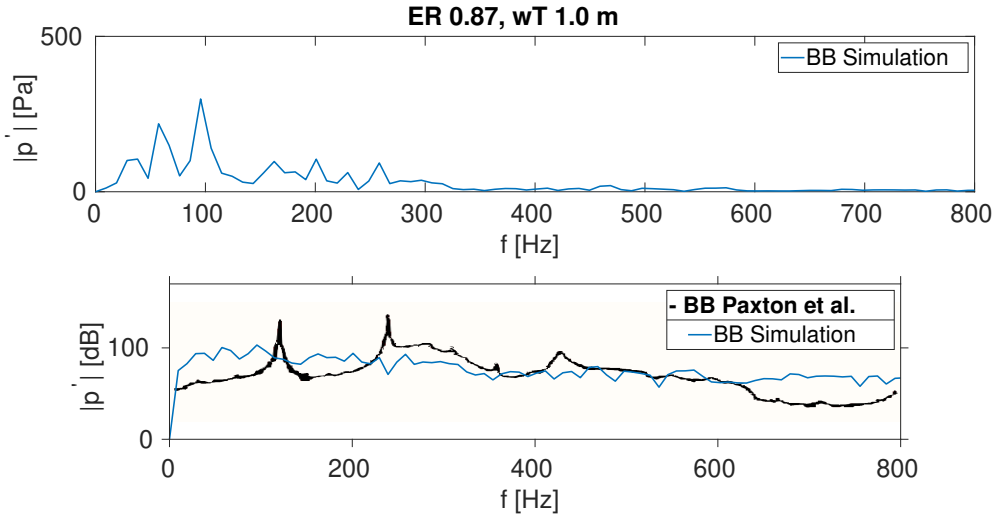

Figure 5.8 – A FFT of the pressure-fluctuations for case 4 at the bluff-body. The top figure is a linear-linear plot, whilst the bottom figure is a log-linear plot with decibels as the y-axis. This is compared with the experiment by Paxton et al. [10] which is represented by the black line.

5.3 Proper Orthogonal Decomposition

In this section the results from performing a POD-analysis on case 2 and 4 will be presented. All of the modes have symmetric color-bars ranging from blue (negative) to red (positive). These coherent structures represent a distribution of amplitudes which vary according to the POD time-coefficients.

In figure 5.9 the first mode for case 2 is presented. This clearly represents the 1L-CC mode as it starts from a minimum and ending at zero. The magnitude in each cell will vary in time which is depicted by the wave function in the bottom left in the same figure. The predominant frequency is 106 Hz accompanied by a lower frequency of 67 Hz. Since there is a clear temperature difference between the inlet through to the bluff-body's trailing edge, and the bluff-bodys trailing edge to the outlet, the POD-analysis could capture these as two frequencies instead of one, but that they are coupled. It is reasonable to say that they are coupled as well since it is still the 1L-CC frequency, just with a different frequency in the domain rather than it having a weighted average frequency. Since the 1L-CC mode is dominant, it could be that the frequency of the pulses are mainly driven by this mode. This

will lead to the vortex-shedding behind the bluff-body to have the same frequency. Hydrodynamic instabilities can also be excited by a multiple of its frequency, such that the BVK frequency is excited by the 1L-CC mode which is stated in [4].

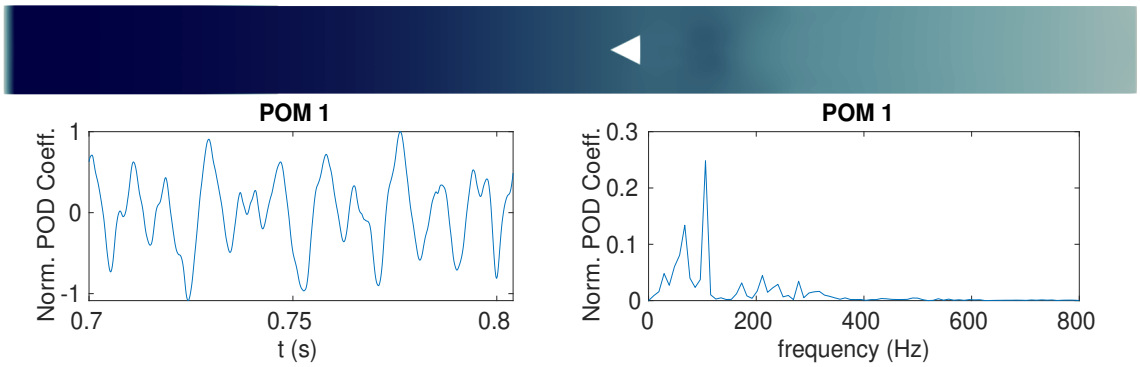

Figure 5.9 – Case 2: Top - Pressure POM-1 coherent structure. Bottom-left - The time coefficients for POM-1. Bottom-right - An FFT of the time coefficients which shows the predominant frequencies corresponding to POM-1's coherent structure. The y-axis is the POD coefficients normalised by the maximum POD coefficient from the most energetic mode.

The second POM can be seen in figure 5.10. This represents a combination of the 1L-CC mode (106 Hz), 3L-CC mode (279 Hz) and the 1L-BB mode (173 Hz). Another frequency that is present is 211 Hz which could be the Strouhal frequency due to the two vortices signified by the white spots which can be seen behind the BB. Another possibility is that it is the 3L-CC mode from the lower frequency present in POM-1 (67 Hz). The support to this suggestion is based on the temperature difference which occurs before and after the combustion region. The minimum pressure increases towards the outlet, but does not quite reach a maximum. Therefore this is less than half a wave and is a linear combination of these previously mentioned modes.

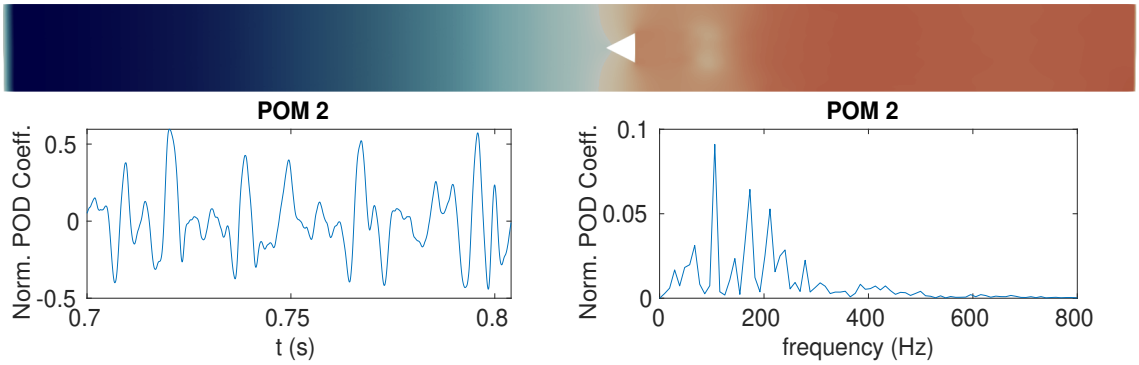

Figure 5.10 – Case 2: Top - Pressure POM-2 coherent structure. Bottom-left - The time coefficients for POM-2. Bottom-right - An FFT of the time coefficients which shows the predominant frequencies corresponding to POM-2's coherent structure. The y-axis is the POD coefficients normalised by the maximum POD coefficient from the most energetic mode.

In the third POM which is seen in figure 5.11, where the 1L-CC mode is not the dominant frequency, instead the 3L-CC mode (279 Hz)is dominant. Other frequencies which are present are 67 Hz, 211 Hz, and 336 Hz. The first two are most likely, as discussed earlier, the 1L-CC and 3L-CC based on the cold part of the combustion chamber. The higher frequency (336 Hz) could represent the fifth longitudinal mode of this series (5L-CC). An alternative explanation is thta it is simply the 3L-CC based on the hot part of the combustion chamber. The pressure decreases until approximately two-thirds towards the outlet, and increases again. It does not reach a maximum which indicates that it is the predominantly the 3L-CC mode. It is possible that the higher frequencies are coupled with transverse modes which can not be seen in the slice presented in the figure. It is not clear if it is a transverse mode or simply the gas-expansion which affects the longitudinal modes.

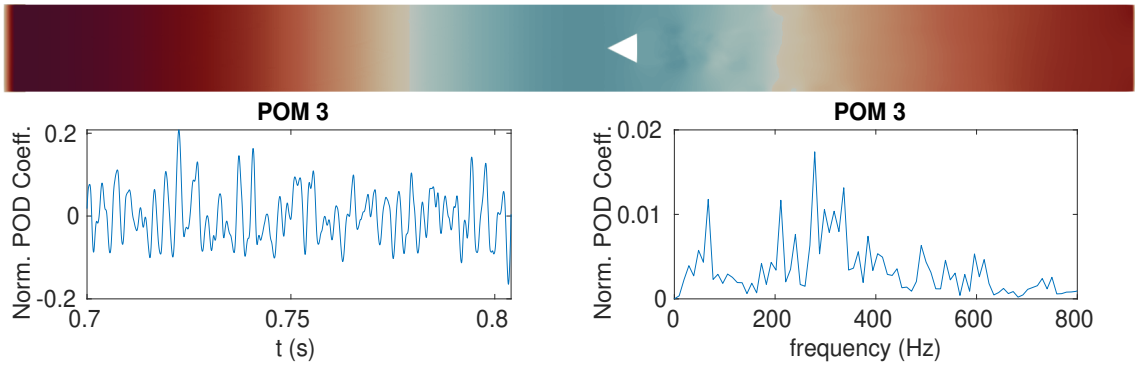

Figure 5.11 – Case 2: Top - Pressure POM-3 coherent structure. Bottom-left - The time coefficients for POM-3. Bottom-right - An FFT of the time coefficients which shows the predominant frequencies corresponding to POM-3's coherent structure. The y-axis is the POD coefficients normalised by the maximum POD coefficient from the most energetic mode.

The fourth POM for case 2 is seen in figure 5.12. This mode has an interesting decrease in pressure at the trailing edge of the bluff body, which increases shortly after, and back to a decrease in pressure once more. Between the inlet and the bluff-body's trailing edge, half a wavelength is present. After the trailing edge, there is a more complex change in pressure. This change in pressure is most likely due to the combination of the 1L-CC mode, vortex-shedding, and the gas-expansion. The vortex-pair creates a low-pressure zone, the combustion will create a high-pressure zone which will initiate the gas-expansion. The point when the gas-expansion overcomes the low-pressure caused by the vortex pair is the conjunction between the recirculation zone and the wake. The increase in pressure close to the outlet is most likely due to the 1L-CC mode. Note that the modes signal over time in the same figure at the bottom left seems to have a high frequency superimposed on the low frequency signal. This is difficult to connect to anything specific as the higher frequencies in the FFT are of very low magnitude and there are many of them. This could be noise or numerical artifacts or a combination of these. Some of these higher frequencies can most likely also be coupled with the transverse modes.

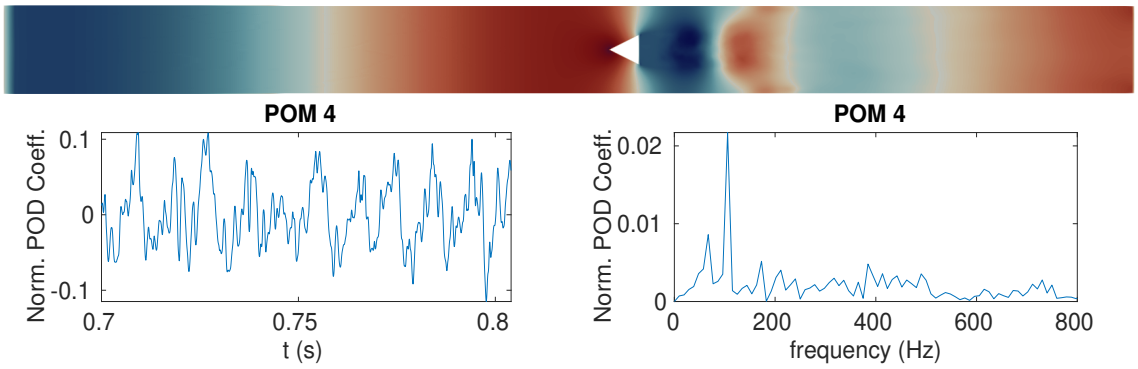

Figure 5.12 – Case 2: Top - Pressure POM-4 coherent structure. Bottom-left - The time coefficients for POM-4. Bottom-right - An FFT of the time coefficients which shows the predominant frequencies corresponding to POM-4's coherent structure. The y-axis is the POD coefficients normalised by the maximum POD coefficient from the most energetic mode.

In case 4 the POD-analysis resulted in different types of modes. This indicates that the increase in equivalence ratio, which increases the temperature and in turn increases the speed of sound, affects the pressure-waves.

For POM-1 the pressure distribution goes from zero at the inlet, to zero at the outlet which is seen in figure 5.13. This indicates that there is a half-wave which is present in i.e. a channel with two open-ends, or two closed-ends. The predominant frequencies in this mode are 86 Hz and 182 Hz. These frequencies are lower than those in case 2 which is contradicting. Since the higher equivalence ratio should lead to an increase in temperature, the frequency should increase since the speed of sound increases. As seen in the experiment by Paxton et al. [10], as the equivalence ratio increases, the frequency increases. From equivalence ratio 0.66 to 0.87, they observed a frequency increase from 91 Hz to 119 Hz for the 1L-CC mode. In the simulations it is seen that the frequency decreases from 106 Hz to 86 Hz. The exact cause of this is not yet known, but it is likely that it has to do with the boundary conditions.

As Poinsot and Veynante mentioned in [4], combustion can introduce a time delay between the energy fed to the acoustic field leading to the possibility for the acoustic field to become amplified (normally these are 90° out of phase). It is possible that the

temperature reached is such that the imaginary part of the wave numbers fluctuation leads to the 3L-CC mode to not be excited. This could indicate that the chosen damping is too high in case 4, or too low in case 3, just missing the required time delay to excite the 3L-CC mode.

Since the frequencies excited in POM-1 include one at 182 Hz, and a lower frequency at 57 Hz, this could indicate the BB's reflected wave between the inlet and bluff-body, together with the 1L-BB mode, could possibly cause this half-wave appearance.

Worth noting is that the time-coefficients seen to change in frequency past approximately 0.8 s. This could be due to a transient behaviour still being present up until that point.

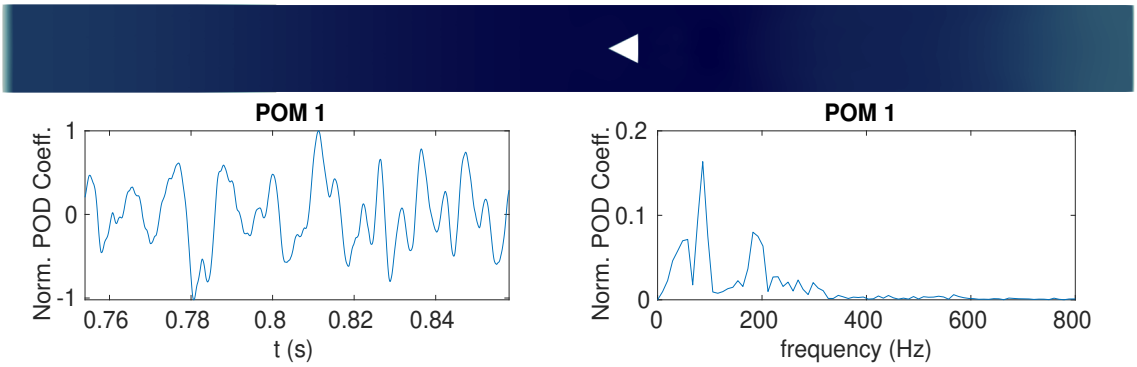

Figure 5.13 – Case 4: Top - Pressure POM-1 coherent structure. Bottom-left - The time coefficients for POM-1. Bottom-right - An FFT of the time coefficients which shows the predominant frequencies corresponding to POM-1's coherent structure. The y-axis is the POD coefficients normalised by the maximum POD coefficient from the most energetic mode.

The second mode in case 4 seen in figure 5.14 is a clear combination of the 1L-CC mode, as well as the 1L-BB mode. Similar to POM-1 in figure 5.13, the signal over time seems to have a super-positioned wave on the wave crests, but this seems to disappear past $t = 0.8$ s. Since it is clearly present in both these modes, it is likely that the simulation had not reached its statistically steady state yet.

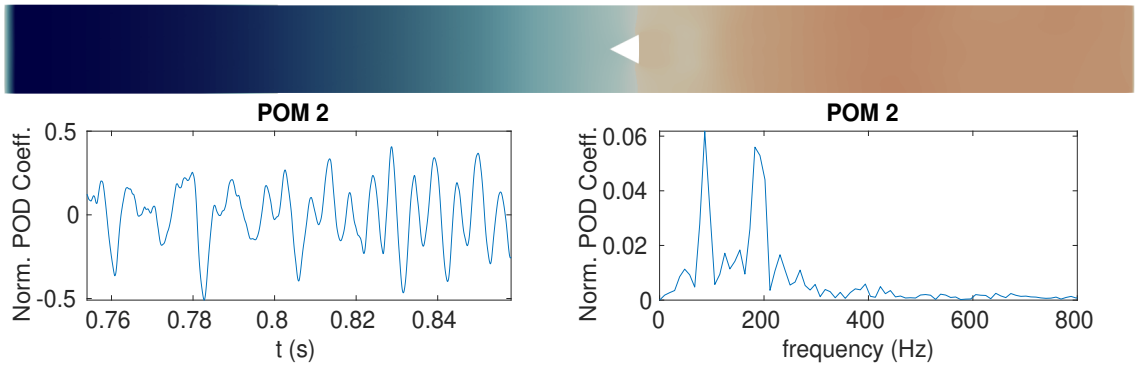

Figure 5.14 – Case 4: Top - Pressure POM-2 coherent structure. Bottom-left - The time coefficients for POM-2. Bottom-right - An FFT of the time coefficients which shows the predominant frequencies corresponding to POM-2's coherent structure. The y-axis is the POD coefficients normalised by the maximum POD coefficient from the most energetic mode.

POM-3 for case 4 seen in figure 5.15 is a combination of the 1L-CC, 1L-BB, 3L-CC and the 3L-BB. These correspond to the frequencies 87 Hz, 183 Hz, 298 Hz and 567 Hz, respectively. The combination of these frequencies seems to create a POM which resembles almost an entire wave-length.

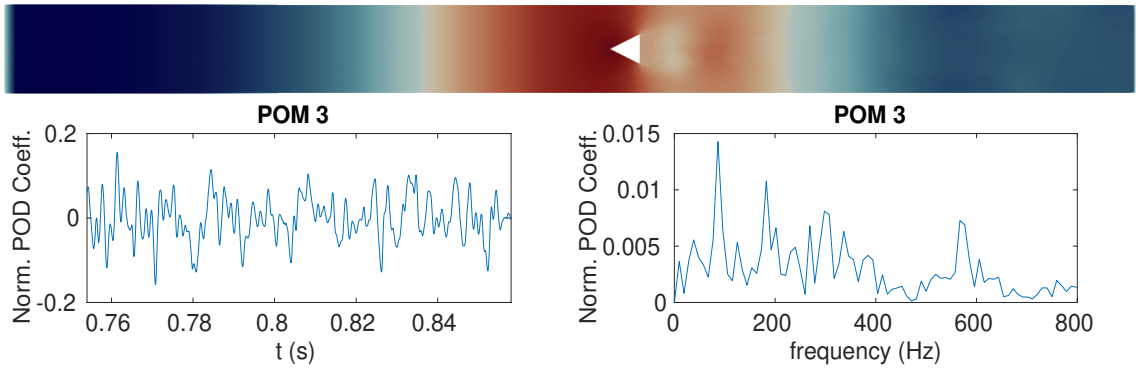

Figure 5.15 – Case 4: Top - Pressure POM-3 coherent structure. Bottom-left - The time coefficients for POM-3. Bottom-right - An FFT of the time coefficients which shows the predominant frequencies corresponding to POM-3's coherent structure. The y-axis is the POD coefficients normalised by the maximum POD coefficient from the most energetic mode.

The last mode, POM-4, can be seen in figure 5.16. This mode consists of multiple low-acoustic-energy frequencies which are the 1L-CC, 1L-BB, 3L-CC, 3L-BB, as well as some extra frequencies such as 38 Hz, 394 Hz, 490 Hz, and 790 Hz. Since these carry very low acoustic-energy, it could be numerical artifacts as well as transverse waves. However, transverse waves usually have high frequencies above 500 Hz, such

that 790 Hz could be a transverse wave. The periodic boundary condition could affect the frequency, resulting in a lower frequency transverse wave since the width of the channel is unknown, interpreted as infinite, by the solver.

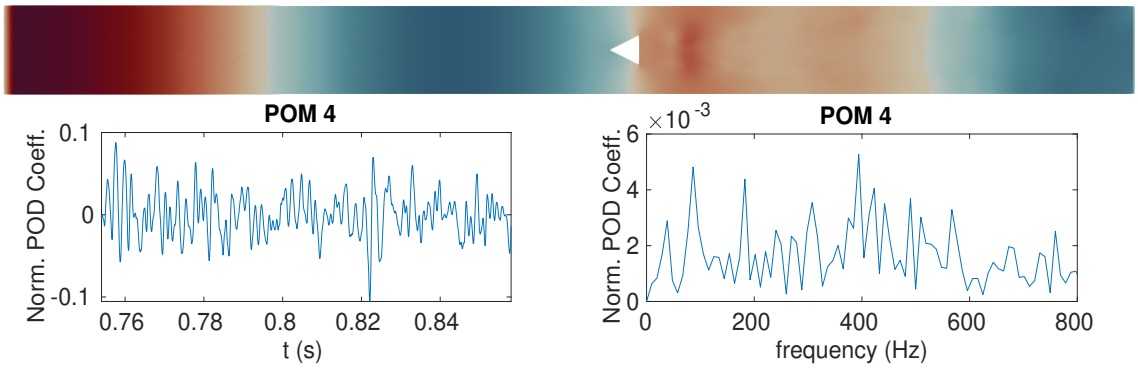

Figure 5.16 – Case 4: Top - Pressure POM-4 coherent structure. Bottom-left - The time coefficients for POM-4. Bottom-right - An FFT of the time coefficients which shows the predominant frequencies corresponding to POM-4's coherent structure. The y-axis is the POD coefficients normalised by the maximum POD coefficient from the most energetic mode.

6 Conclusion

A coarse boundary condition sensitivity analysis was performed with the outlet conditions for pressure which include:

- Pressure - waveTransmissive, infinite pressure field 101300 Pa, length to infinite pressure field 0.1 m.
- Pressure - waveTransmissive, infinite pressure field 101300 Pa, length to infinite pressure field 1.0 m.
- Pressure - fixedValue, imposed pressure set to 101300 Pa.

The first two boundary conditions were tested on both equivalence ratios (0.66 and 0.87). The results indicate a non-trivial solution since the pressure fluctuations were dampened between case 1 and 2, but increased for case 3 and 4.

All cases for the lower equivalence ratio over-estimated the pressure fluctuations, whilst cases with the higher equivalence ratio under-estimated the pressure fluctuations.

Using the specified distance 0.1 m seems to allow the 3L-CC mode to be excited, whilst 1.0 m seems to allow the 1L-CC mode to be excited.

The flame-dynamics indicate that the amplitude of the pressure fluctuations is coupled with the pulsating necking behaviour of the flame. A more quantitative analysis is needed to connect this behaviour to the 3L-CC mode. However, the theory of compressions (crests of the pressure-wave) and rarefactions (trough of the pressure-wave), together with the experimental results from [10] in conjunction with the

simulation results indicate that it could be the aforementioned mode which is the cause of the pulsating necking behaviour.

The predominant frequencies were slightly higher for case 1 and 2, with case 2 being the better fit when compared to [10]. The frequencies observed in the FFT for case 2 were higher than that of the experiments, where the 1L-CC was more excited than 3L-CC, which differs from their experimental results. However, case 1 led to 3L-CC being more excited, which indicates that the optimal boundary condition for pressure at the outlet is somewhere between 0.1 m and 1.0 m.

The frequencies observed in case 4 were lower than those in the experiment by[10]. The expected frequency was around 119 Hz, however a frequency of 95 Hz was observed. None of the frequencies were excited the magnitude which was seen in the experiment. The 1L-BB and 3L-CC modes had not been fed enough energy by the combustion.

The POD analysis proved useful to witness the pressure-modes with highest energy. For case 2, the modes consisted of a clear 1L-CC mode (POM-1), followed by a combination of 1L-CC, 1L-BB and 3L-CC modes (POM-2). POM-3 indicated that the 3L-CC mode was dominant with the 1L-CC and 1L-BB also being present. Lastly the POM-4 was predominantly a combination of the 1L-CC, with a lot of influence from higher frequencies which could be transverse frequencies or numerical artifacts. Figure 5.12 showed that the vortex-shedding could be controlled by the 1L-CC mode, indicated by the low- and high-pressure zones behind the bluff-body.

For case 4, the modes were not as clear. The modes included a combination of the 1L-CC and 1L-BB modes (POM-1) and resembled the coherent structure similar to a half-wave. The second mode was a clearer combination of the 1L-CC and 1L-BB modes (POM-2), whilst the third mode was a combination of several frequencies but predominantly 1L-CC, 1L-BB, 3L-CC and 3L-BB (POM-3). The fourth mode consisted of a lot of noise as well as 1L-CC, 1L-BB, 3L-CC and 3L-BB (POM-4).

7 Future Work

The simulations performed in this master's thesis did not reach to the same results as that of Paxton et al. [10]. Therefore further investigation on how the boundary conditions affect the simulation is required to see if the simulation converges towards the experimental results.

In addition to the current equivalence ratios studied, an equivalence ratio between 0.66 and 0.87 will be studied. It would be interesting to observe the stable-, transition- and limit-cycle regions in the simulation results.

Furthermore, to reduce computational cost in the future when performing thermoacoustic analysis, an expression, or optimized procedure will be developed to impose a boundary condition which is satisfactory to reduce the resources needed for a similar study.

A simulation with a larger computational cost will be performed which includes a part of the cavity with a course mesh to be able to investigate flames expansion into the cavity, as well as to increase the understanding of the boundary conditions effect on the thermoacoustics. Including the cavity will enable a more detailed comparison of the pressure-,velocity-, and temperature-waves amplitude and frequency at the outlet of the combustion chamber.

Figure B.2 which was obtained from acoustic theory on the input acoustic impedance in a system will be further investigated, if it is possible to implement this knowledge into the decision of which boundary conditions to be imposed at the outlet.

Lastly, how the velocity and temperature boundary conditions at the outlet affect the thermoacoustics will also be explored.

The thermoacoustic instability has been investigated, however, not with the appropriate boundary conditions. The conditions for which the realistic thermoacoustic behaviour emerges will be further investigated to increase the knowledge and understanding of both thermoacoustics, and outlet boundary conditions affect on thermoacoustics. One way to potentially find a pattern in the thermoacoustic behaviour, is to create an attractor which couples the non-linear behaviour in the feedback loop.

Currently, the longitudinal modes have been of largest focus, whereas the transverse modes are also of great interest. These will also be investigated in future work.

Another necessary part is to connect the results to the equations for the purpose of increasing the understanding of the equations to be able to predict the behaviour.

In the present study, n-dodecane was used. The skeletal reaction mechanism is expensive, and propane could be used with the Z77 skeletal reaction mechanism developed by Zettervall [17], which has been widely studied thus leading to large amount of possibilities for validation.

Another way to reduce the computational cost is to use dynamic load bearing (DLB) which divides cells to the processors more qualitatively, rather than quantitatively. This would reduce a single processor to act as a bottle-neck for the entire simulation.

Since thermoacoustics is the coupling between heat release, and acoustics, the temperature and velocity will be investigated further using POD. The hope is to see if coherent structures in the pressure, temperature and velocity appear together in a pattern. If these structures appear in pairs, or not.

Dynamic mode decomposition (DMD) is another method to investigate different modes. Instead of a decomposition based on energy, it decomposites based on frequency, allowing the researcher to investigate desired frequencies which are expected due to experimental results. Ghani et al. [5] used DMD to investigate both the

1Lx-CC mode (longitudinal mode known as the buzz mode) and the 1Lx-2Ty mode (transverse mode known as the screech mode). This was compared to the Volvo Validation Rig by [26] to investigate the previously mentioned modes successfully.

The large scope of the present study is to increase the knowledge and understanding of thermoacoustics in order to reduce the possible damage caused in a combustion chamber. The challenges in the future is to strive for the more sustainable society which requires higher efficiencies, cleaner emissions and thus also different types of fuels are required. Higher efficiencies and cleaner emissions usually come paired, however, currently it is at the expense of the combustion chamber and overall the engines lifetime [4], [5]. Some of the fuels which shall be studied include *Jet-A*, *JP-5*, *C-1* and *C-5*. The last two are biofuels based on iso-paraffins and n-paraffins.

References

[1] I. A. T. A. (IATA). "Offsetting co2 emissions with corsia." (2023), [Online]. Available: https://www.iata.org/en/programs/environment/corsia/ (visited on 05/26/2023).

[2] I. A. T. A. (IATA). "Developing sustainable aviation fuel (saf)." (2023), [Online]. Available: https://www.iata.org/en/programs/environment/sustainable-aviation-fuels/ (visited on 05/26/2023).

[3] T. Lieuwen, S. Shanbhogue, S. Khosla, and C. Smith, "Dynamics of Bluff Body Flames Near Blowoff," en, in *45th AIAA Aerospace Sciences Meeting and Exhibit*, Reno, Nevada: American Institute of Aeronautics and Astronautics, Jan. 2007, ISBN: 978-1-62410-012-3. DOI: 10.2514/6.2007-169. [Online]. Available: https://arc.aiaa.org/doi/10.2514/6.2007-169 (visited on 02/23/2023).

[4] T. Poinsot and D. Veynante, *Theoretical and Numerical Combustion*. Edwards, 2001, ISBN: 9781930217058. [Online]. Available: https://books.google.se/books?id=HMvCQgAACAAJ.

[5] A. Ghani, T. Poinsot, L. Gicquel, and G. Staffelbach, "LES of longitudinal and transverse self-excited combustion instabilities in a bluff-body stabilized turbulent premixed flame," en, *Combustion and Flame*, vol. 162, no. 11, pp. 4075–4083, Nov. 2015, ISSN: 00102180. DOI: 10.1016/j.combustflame.2015.08.024. [Online]. Available: https://linkinghub.elsevier.com/retrieve/pii/S0010218015002989 (visited on 05/20/2023).

[6] F. Nicoud and T. Poinsot, "Thermoacoustic instabilities: Should the Rayleigh criterion be extended to include entropy changes?" en, *Combustion and Flame*, vol. 142, no. 1-2, pp. 153–159, Jul. 2005, ISSN: 00102180. DOI: 10.1016/j.combustflame.2005.02.013. [Online]. Available: https://linkinghub.elsevier.com/retrieve/pii/S0010218005000775 (visited on 02/23/2023).

[7] K. Bengtsson, "Thermoacoustic instabilities in a gas turbine combustor," M.S. thesis, The Royal Institute of Technology, 2017.

[8] H. K. Versteeg and W. Malalasekera, *An introduction to computational fluid dynamics: the finite volume method*. Pearson education, 2007.

[9] S. Kostka, A. C. Lynch, B. C. Huelskamp, B. V. Kiel, J. R. Gord, and S. Roy, "Characterization of flame-shedding behavior behind a bluff-body using proper orthogonal decomposition," en, *Combustion and Flame*, vol. 159, no. 9, pp. 2872–2882, Sep. 2012, ISSN: 00102180. DOI: 10.1016/j.combustflame.2012.03.021. [Online]. Available: https://

linkinghub.elsevier.com/retrieve/pii/S0010218012001095 (visited on 02/23/2023).

[10] B. T. Paxton, C. A. Fugger, A. S. Tomlin, and A. W. Caswell, "Experimental Investigation of Fuel Chemistry on Combustion Instabilities in a Premixed Bluff-Body Combustor," en, in *AIAA Scitech 2020 Forum*, Orlando, FL: American Institute of Aeronautics and Astronautics, Jan. 2020, ISBN: 978-1-62410-595-1. DOI: 10.2514/6.2020-0174. [Online]. Available: https://arc.aiaa.org/doi/10.2514/6.2020-0174 (visited on 02/23/2023).

[11] C. Fureby, "The Volvo Validation Rig – A Comparative Study of Large Eddy Simulation Combustion Models at Different Operating Conditions," en, in *2018 AIAA Aerospace Sciences Meeting*, Kissimmee, Florida: American Institute of Aeronautics and Astronautics, Jan. 2018, ISBN: 978-1-62410-524-1. DOI: 10.2514/6.2018-0149. [Online]. Available: https://arc.aiaa.org/doi/10.2514/6.2018-0149 (visited on 02/23/2023).

[12] C. Fureby, "A Large Eddy Simulation (LES) Study of the VOLVO and AFRL Bluff Body Combustors at Different Operating Conditions," en, in *AIAA Scitech 2019 Forum*, San Diego, California: American Institute of Aeronautics and Astronautics, Jan. 2019, ISBN: 978-1-62410-578-4. DOI: 10.2514/6.2019-0453. [Online]. Available: https://arc.aiaa.org/doi/10.2514/6.2019-0453 (visited on 02/23/2023).

[13] T. Yao, Y. Pei, B.-J. Zhong, S. Som, T. Lu, and K. H. Luo, "A compact skeletal mechanism for n-dodecane with optimized semi-global low-temperature chemistry for diesel engine simulations," *Fuel*, vol. 191, pp. 339–349, 2017, ISSN: 0016-2361. DOI: https://doi.org/10.1016/j.fuel.2016.11.083. [Online]. Available: https://www.sciencedirect.com/science/article/pii/S001623611631184X.

[14] S. J. Shanbhogue, S. Husain, and T. Lieuwen, "Lean blowoff of bluff body stabilized flames: Scaling and dynamics," en, *Progress in Energy and Combustion Science*, vol. 35, no. 1, pp. 98–120, Feb. 2009, ISSN: 03601285. DOI: 10.1016/j.pecs.2008.07.003. [Online]. Available: https://linkinghub.elsevier.com/retrieve/pii/S0360128508000427 (visited on 02/23/2023).

[15] M. Mendez, M. Nardo, and C. Benocci, "Running fineopen43 simulations at vki: A tutorial and a collection of scripts," Mar. 2017. DOI: 10.13140/RG.2.2.19214.31041.

[16] E. Zukoski, "Combustion instability sustained by unsteady vortex combustion," en, in *21st Joint Propulsion Conference*, Monterey,CA,U.S.A.: American Institute of Aeronautics and Astronautics, Jul. 1985. DOI: 10.2514/6.1985-1248. [Online]. Available: https://arc.aiaa.org/doi/10.2514/6.1985-1248 (visited on 02/23/2023).

[17] N. Zettervall, K. Nordin-Bates, E. Nilsson, and C. Fureby, "Large Eddy Simulation of a premixed bluff body stabilized flame using global and skeletal reaction mechanisms," en, *Combustion and Flame*, vol. 179, pp. 1–22, May 2017, ISSN: 00102180. DOI: 10.1016/j.combustflame.2016.12.007. [Online]. Available: https://linkinghub.elsevier.com/retrieve/pii/S0010218016303704 (visited on 02/23/2023).

[18] C. Fureby, "Large Eddy Simulation of turbulent reacting flows with conjugate heat transfer and radiative heat transfer," en, *Proceedings of the Combustion Institute*, vol. 38, no. 2, pp. 3021–3029, 2021, ISSN: 15407489. DOI: 10.1016/j.proci.2020.06.285. [Online]. Available: https://linkinghub.elsevier.com/retrieve/pii/S1540748920303771 (visited on 02/23/2023).

[19] C. A. Fugger, T. Yi, J. Sykes, *et al.*, "The Structure and Dynamics of a Bluff-Body Stabilized Premixed Reacting Flow," en, in *2018 AIAA Aerospace Sciences Meeting*, Kissimmee, Florida: American Institute of Aeronautics and Astronautics, Jan. 2018, ISBN: 978-1-62410-524-1. DOI: 10.2514/6.2018-1190. [Online]. Available: https://arc.aiaa.org/doi/10.2514/6.2018-1190 (visited on 02/23/2023).

[20] C. A. Fugger, S. Roy, A. W. Caswell, B. A. Rankin, and J. R. Gord, "Structure and dynamics of CH2O, OH, and the velocity field of a confined bluff-body premixed flame, using simultaneous PLIF and PIV at 10 kHz.," en, *Proceedings of the Combustion Institute*, vol. 37, no. 2, pp. 1461–1469, 2019, ISSN: 15407489. DOI: 10.1016/j.proci.2018.05.014. [Online]. Available: https://linkinghub.elsevier.com/retrieve/pii/S1540748918300142 (visited on 02/23/2023).

[21] C. A. Fugger, J. Sykes, T. Gallagher, B. Rankin, and A. W. Caswell, "Corner Vortex Structures: Spanwise Imaging of a Confined, Premixed Bluff Body Stabilized Flame," en, in *AIAA Scitech 2020 Forum*, Orlando, FL: American Institute of Aeronautics and Astronautics, Jan. 2020, ISBN: 978-1-62410-595-1. DOI: 10.2514/6.2020-0435. [Online]. Available: https://arc.aiaa.org/doi/10.2514/6.2020-0435 (visited on 02/23/2023).

[22] B. T. Paxton, C. A. Fugger, B. A. Rankin, and A. W. Caswell, "Development and Characterization of an Experimental Arrangement for Studying Bluff-Body-Stabilized Turbulent Premixed Propane-Air Flames," en, in *AIAA Scitech 2019 Forum*, San Diego, California: American Institute of Aeronautics and Astronautics, Jan. 2019, ISBN: 978-1-62410-578-4. DOI: 10.2514/6.2019-0118. [Online]. Available: https://arc.aiaa.org/doi/10.2514/6.2019-0118 (visited on 03/30/2023).

[23] S. Shanbhogue, D. Plaks, and T. Lieuwen, "The K-H Instability of Reacting, Acoustically Excited Bluff Body Shear Layers," en, in *43rd AIAA/ASME/SAE/ASEE Joint Propulsion Conference & Exhibit*, Cincinnati, OH: American Institute of Aeronautics and Astronautics, Jul. 2007, ISBN: 978-1-62410-011-6. DOI: 10.2514/6.2007-5680. [Online]. Available: http:

//arc.aiaa.org/doi/abs/10.2514/6.2007-5680 (visited on 02/23/2023).

[24] S. Shanbhogue and T. Lieuwen, "Studies on the Vorticity Field of Harmonically Excited Bluff-Body Flames," en, in *46th AIAA Aerospace Sciences Meeting and Exhibit*, Reno, Nevada: American Institute of Aeronautics and Astronautics, Jan. 2008, ISBN: 978-1-62410-128-1. DOI: 10.2514/6.2008-122. [Online]. Available: https://arc.aiaa.org/doi/10.2514/6.2008-122 (visited on 02/23/2023).

[25] S. Shanbhogue, D.-H. Shin, S. Hemchandra, D. Plaks, and T. Lieuwen, "Flame-sheet dynamics of bluff-body stabilized flames during longitudinal acoustic forcing," en, *Proceedings of the Combustion Institute*, vol. 32, no. 2, pp. 1787–1794, 2009, ISSN: 15407489. DOI: 10.1016/j.proci.2008.06.034. [Online]. Available: https://linkinghub.elsevier.com/retrieve/pii/S1540748908000564 (visited on 02/23/2023).

[26] A. Sjunnesson, P. Henrikson, and C. Lofstrom, "CARS measurements and visualization of reacting flows in a bluff body stabilized flame," en, in *28th Joint Propulsion Conference and Exhibit*, Nashville,TN,U.S.A.: American Institute of Aeronautics and Astronautics, Jul. 1992. DOI: 10.2514/6.1992-3650. [Online]. Available: https://arc.aiaa.org/doi/10.2514/6.1992-3650 (visited on 02/23/2023).

[27] R. Erickson, M. Soteriou, and P. Mehta, "The Influence of Temperature Ratio on the Dynamics of Bluff Body Stabilized Flames," en, in *44th AIAA Aerospace Sciences Meeting and Exhibit*, Reno, Nevada: American Institute of Aeronautics and Astronautics, Jan. 2006, ISBN: 978-1-62410-039-0. DOI: 10.2514/6.2006-753. [Online]. Available: https://arc.aiaa.org/doi/10.2514/6.2006-753 (visited on 02/23/2023).

[28] R. Erickson and M. Soteriou, "The influence of reactant temperature on the dynamics of bluff body stabilized premixed flames," en, *Combustion and Flame*, vol. 158, no. 12, pp. 2441–2457, Dec. 2011, ISSN: 00102180. DOI: 10.1016/j.combustflame.2011.05.006. [Online]. Available: https://linkinghub.elsevier.com/retrieve/pii/S0010218011001520 (visited on 02/23/2023).

[29] B. Emerson, J. Lundrigan, J. O'Connor, D. Noble, and T. Lieuwen, "Dependence of the Bluff Body Wake Structure on Flame Temperature Ratio," en, in *49th AIAA Aerospace Sciences Meeting including the New Horizons Forum and Aerospace Exposition*, Orlando, Florida: American Institute of Aeronautics and Astronautics, Jan. 2011, ISBN: 978-1-60086-950-1. DOI: 10.2514/6.2011-597. [Online]. Available: https://arc.aiaa.org/doi/10.2514/6.2011-597 (visited on 02/23/2023).

[30] C. Smith, D. Nickolaus, T. Leach, B. Kiel, and K. Garwick, "LES Blowout Analysis of Premixed Flow Past V-gutter Flameholder," en, in *45th AIAA Aerospace Sciences Meeting and Exhibit*, Reno, Nevada: American Institute of Aeronautics and Astronautics, Jan. 2007, ISBN: 978-1-62410-012-3. DOI:

10.2514/6.2007-170. [Online]. Available: https://arc.aiaa.org/doi/10.2514/6.2007-170 (visited on 02/23/2023).

[31] L. Beranek and T. Mellow, "Chapter two - the wave equation and solutions," in *Acoustics (Second Edition)*, L. Beranek and T. Mellow, Eds., Second Edition, Academic Press, 2019, pp. 25–79, ISBN: 978-0-12-815227-0. DOI: https://doi.org/10.1016/B978-0-12-815227-0.00002-9. [Online]. Available: https://www.sciencedirect.com/science/article/pii/B9780128152270000029.

[32] L. Beranek and T. Mellow, "Chapter four - acoustic components," in *Acoustics (Second Edition)*, L. Beranek and T. Mellow, Eds., Second Edition, Academic Press, 2019, pp. 143–229, ISBN: 978-0-12-815227-0. DOI: https://doi.org/10.1016/B978-0-12-815227-0.00004-2. [Online]. Available: https://www.sciencedirect.com/science/article/pii/B9780128152270000042.

[33] L. Beranek and T. Mellow, "Chapter ten - sound in enclosures," in *Acoustics (Second Edition)*, L. Beranek and T. Mellow, Eds., Second Edition, Academic Press, 2019, pp. 511–545, ISBN: 978-0-12-815227-0. DOI: https://doi.org/10.1016/B978-0-12-815227-0.00010-8. [Online]. Available: https://www.sciencedirect.com/science/article/pii/B9780128152270000108.

[34] L. Kinsler and A. Frey, *Fundamentals of Acoustics*. Wiley, 1950. [Online]. Available: https://books.google.se/books?id=EU41AAAAMAAJ.

[35] S. H. van Buren, *Acoustic and thermal characterization of quarter-wave resonators*, en, 2021.

[36] S. Candel, S. Ducruix, D. Durox, and D. Veynante, *Lecture notes in combustion dynamics: Analysis and control - modeling*, May 2001.

[37] T. Baritaud, T. Poinsot, M. Baum, and C. de recherche sur la combustion turbulente (France), *Direct Numerical Simulation for Turbulent Reacting Flows*. Editions Technip, 1996, ISBN: 9782710806981. [Online]. Available: https://books.google.se/books?id=St9WRs5vOoMC.

[38] A. S. Tomlin, C. A. Fugger, and A. W. Caswell, "Thermoacoustic Instabilities in a Three Bluff Body Flow," en, in *AIAA Scitech 2020 Forum*, Orlando, FL: American Institute of Aeronautics and Astronautics, Jan. 2020, ISBN: 978-1-62410-595-1. DOI: 10.2514/6.2020-1880. [Online]. Available: https://arc.aiaa.org/doi/10.2514/6.2020-1880 (visited on 02/23/2023).

[39] F. Franchetti and M. Püschel, "FFT (Fast Fourier Transform)," in *Encyclopedia of Parallel Computing*, D. Padua, Ed., Boston, MA: Springer US, 2011, pp. 658–671, ISBN: 978-0-387-09766-4. DOI: 10.1007/978-0-387-09766-4_243. [Online]. Available: https://doi.org/10.1007/978-0-387-09766-4_243.

[40] T. M. Peters and J. H. T. Bates, "The Discrete Fourier Transform and the Fast Fourier Transform," in *The Fourier Transform in Biomedical Engineering*, T. M. Peters and J. Williams, Eds., Boston, MA: Birkhäuser Boston, 1998, pp. 175–194, ISBN: 978-1-4612-0637-8. DOI: 10.1007/978-1-4612-0637-8_6. [Online]. Available: https://doi.org/10.1007/978-1-4612-0637-8_6.

[41] OpenFOAM Ltd. "Wavetransmissivefvpatchfield¡ type ¿ class template reference." (), [Online]. Available: https://www.openfoam.com/documentation/guides/latest/api/classFoam_1_1waveTransmissiveFvPatchField.html.

[42] E. Garnier, N. Adams, and P. Sagaut, *Large Eddy Simulation for Compressible Flows* (Scientific Computation), en, J.-J. Chattot, P. Colella, W. Eist, *et al.*, Eds. Dordrecht: Springer Netherlands, 2009, ISBN: 978-90-481-2819-8. DOI: 10.1007/978-90-481-2819-8. [Online]. Available: http://link.springer.com/10.1007/978-90-481-2819-8 (visited on 05/19/2023).

[43] N. D. Katopodes, "Chapter9 - methods for incompressible viscous flow," in *Free-Surface Flow*, N. D. Katopodes, Ed., Butterworth-Heinemann, 2019, pp. 568–613, ISBN: 978-0-12-815485-4. DOI: https://doi.org/10.1016/B978-0-12-815485-4.00015-2. [Online]. Available: https://www.sciencedirect.com/science/article/pii/B9780128154854000152.

[44] S. B. Pope, *Turbulent Flows*. Cambridge University Press, 2000. DOI: 10.1017/CBO9780511840531.

[45] J. B. Joshi, K. Nandakumar, A. W. Patwardhan, *et al.*, "2 - computational fluid dynamics," in *Advances of Computational Fluid Dynamics in Nuclear Reactor Design and Safety Assessment*, ser. Woodhead Publishing Series in Energy, J. B. Joshi and A. K. Nayak, Eds., Woodhead Publishing, 2019, pp. 21–238, ISBN: 978-0-08-102337-2. DOI: https://doi.org/10.1016/B978-0-08-102337-2.00002-X. [Online]. Available: https://www.sciencedirect.com/science/article/pii/B978008102337200002X.

[46] X. You, F. N. Egolfopoulos, and H. Wang, "Detailed and simplified kinetic models of n-dodecane oxidation: The role of fuel cracking in aliphatic hydrocarbon combustion," *Proceedings of the Combustion Institute*, vol. 32, no. 1, pp. 403–410, 2009, ISSN: 1540-7489. DOI: https://doi.org/10.1016/j.proci.2008.06.041. [Online]. Available: https://www.sciencedirect.com/science/article/pii/S1540748908000898.

[47] C. Westbrook, W. Pitz, O. Herbinet, H. Curran, and E. Silke, "A comprehensive detailed chemical kinetic reaction mechanism for combustion of n-alkane hydrocarbons from n-octane to n-hexadecane," *Combustion and Flame*,

vol. 156, pp. 181–199, Jan. 2009. DOI: 10.1016/j.combustflame.2008.07.014.

[48] H. Wang, H. Wang, F. Gao, P. Zhou, and Z. (Zhai, "Literature review on pressure–velocity decoupling algorithms applied to built-environment cfd simulation," *Building and Environment*, vol. 143, pp. 671–678, 2018, ISSN: 0360-1323. DOI: https://doi.org/10.1016/j.buildenv.2018.07.046. [Online]. Available: https://www.sciencedirect.com/science/article/pii/S0360132318304542.

[49] R. Issa, "Solution of the implicitly discretised fluid flow equations by operator-splitting," *Journal of Computational Physics*, vol. 62, no. 1, pp. 40–65, 1986, ISSN: 0021-9991. DOI: https://doi.org/10.1016/0021-9991(86)90099-9. [Online]. Available: https://www.sciencedirect.com/science/article/pii/0021999186900999.

A Appendix 1. Segregated Solvers

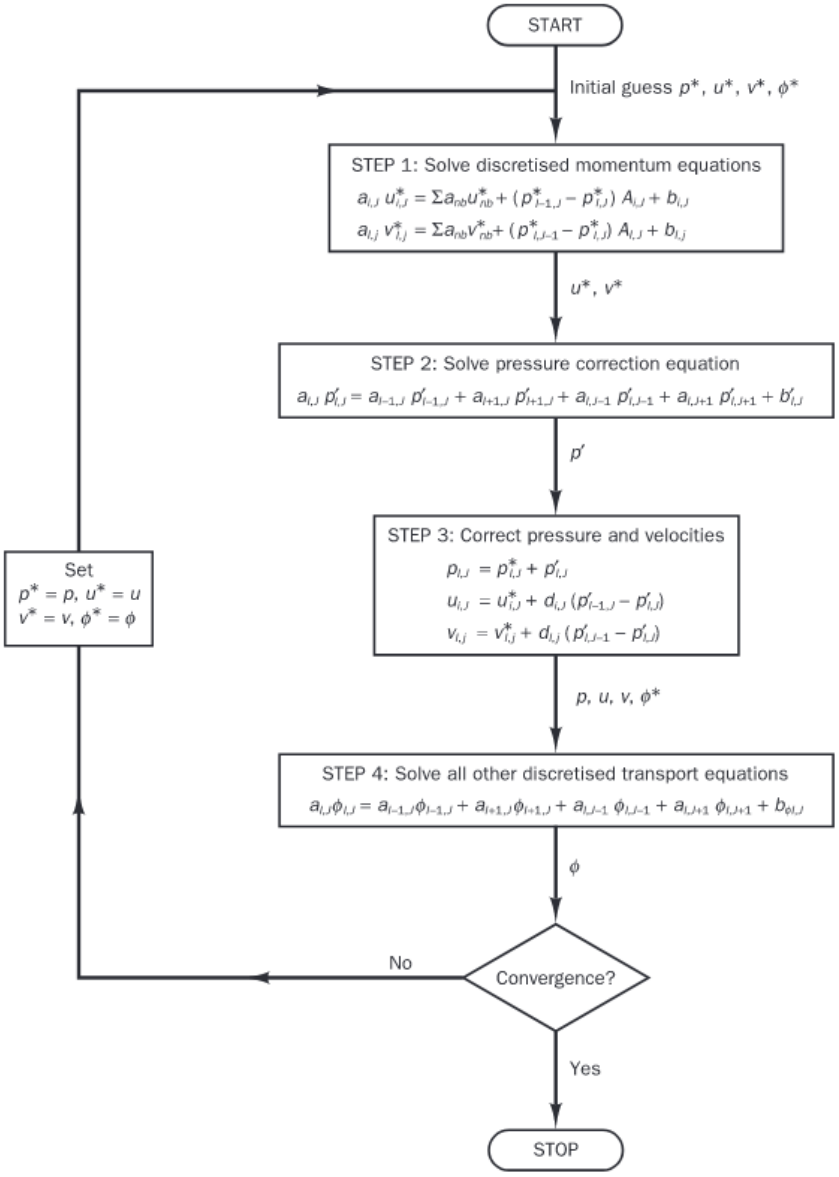

Figure A.1 – The SIMPLE-algorithm. [8]

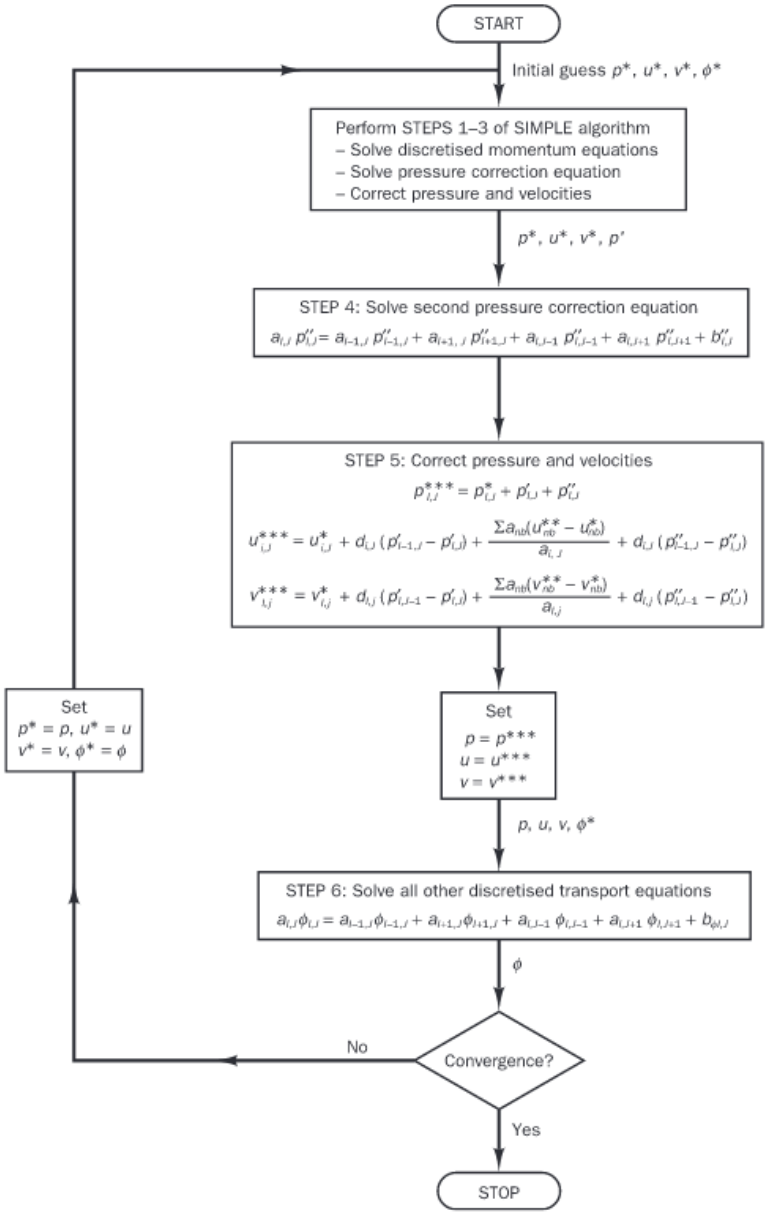

Figure A.2 – The PISO-algorithm. [8]

B Appendix 2. Input Acoustic Impedance

The outlet's input of acoustic impedance is of interest to study. Using equation 2.13, a surf-plot was obtained by allowing the length of the channel and the frequency to change. This plot can be seen in figures B.1 and B.2.

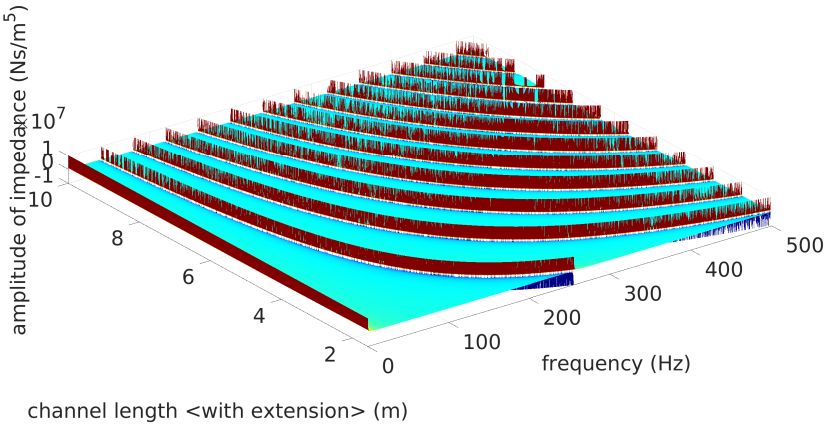

Figure B.1 – The acoustic impedance surf plot showing all three dimensions, amplitude of impedance, channel extension, and frequency. Note that the outlet only changes the imaginary part of the impedance (reactance).

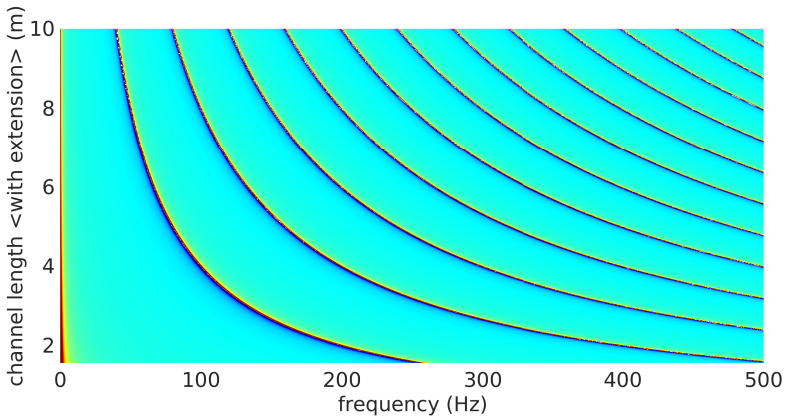

Figure B.2 – The acoustic impedance rotated to see which frequencies are expected to be excited in terms of channel extension.

The input acoustic impedance to the system due to the outlet's boundary condition

changes dramatically in the form of co-tangent periodic curves. These curves increase in frequency as the channel length is extended, and naturally the longer the channel, the lower the frequencies can be.

Since the waveTransmissive-BC's chosen distance to the infinite field determines the impedance imposed at the outlet, one can also think of it as an increase in acoustic mass, or a displacement of the pressure-node [32]. The input impedance is the imaginary part of the impedance, which affects how much acoustic energy can be stored, and whether it is reflected or transmitted. However, since the waveTransmissive BC is a linear damping of the chosen variable, it is likely that the non-linear effects are caused by some quantity in the system being damped which has a non-linear coupling with the thermo-acoustic instability.